

# Octahedral Tilt-Driven Phase Transitions in BaZrS<sub>3</sub> Chalcogenide Perovskite

Prakriti Kayastha, Erik Fransson, Paul Erhart, and Lucy Whalley\*



Cite This: *J. Phys. Chem. Lett.* 2025, 16, 2064–2071



Read Online

ACCESS |



Metrics & More

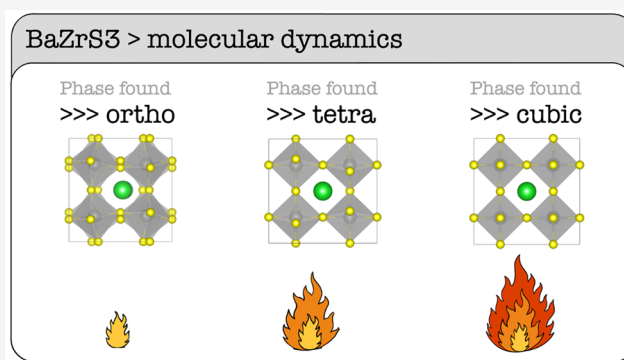


Article Recommendations



Supporting Information

**ABSTRACT:** Chalcogenide perovskites are lead-free materials for potential photovoltaic or thermoelectric applications. BaZrS<sub>3</sub> is the most-studied member of this family due to its superior thermal and chemical stability, desirable optoelectronic properties, and low thermal conductivity. Phase transitions in BaZrS<sub>3</sub> remain underexplored in the literature, as most experimental characterizations of this material have been performed at ambient conditions where the orthorhombic *Pnma* phase is reported to be stable. In this work, we study the dynamics of BaZrS<sub>3</sub> across a range of temperatures and pressures using an accurate machine learning interatomic potential trained with data from hybrid density functional theory calculations. At 0 Pa, we find a first-order phase transition from the orthorhombic to tetragonal *I4/mcm* phase at 610 K, and a second-order transition from the tetragonal to the cubic *Pm3m* phase at 880 K. The tetragonal phase is stable over a larger temperature range at higher pressures. To confirm the validity of our model we compare our results with a range of published experimental data and report a prediction for the X-ray diffraction pattern as a function of temperature.



Chalcogenide perovskites have gained relevance as lead-free photovoltaic absorber materials as they exhibit strong light absorption and dielectric screening alongside desirable defect properties.<sup>1–9</sup> BaZrS<sub>3</sub> is the most studied member of this family with research efforts towards material synthesis at moderate temperatures, band gap engineering, and a proof-of-concept solar cell.<sup>10–19</sup> BaZrS<sub>3</sub> has also been explored as a potential thermoelectric material as it displays fast electronic transport coupled with low thermal conductivity, leading to record-high *zT* values among reported halide and chalcogenide perovskite materials.<sup>20–22</sup>

While BaZrS<sub>3</sub> is reported to retain stability in a perovskite structure above 1000 K, the vast majority of materials characterization is carried out at ambient conditions.<sup>10,11,23–25</sup>

At room temperature, the consensus is that BaZrS<sub>3</sub> is stable in an orthorhombic *Pnma* perovskite structure, as confirmed by both experimental and computational studies.<sup>13,21,26–30</sup> Above this temperature, the picture is less clear. Recent temperature-dependent X-ray diffraction (XRD) measurements show a discontinuous change in the lattice parameters at high temperature, indicating a first-order phase transition.<sup>23,31,32</sup> However a temperature-dependent Raman spectroscopy study does not confirm this observation,<sup>33</sup> likely due to the structural and dynamic similarity of perovskite phases coupled with significant thermal broadening.

Many ABX<sub>3</sub> perovskites undergo tilt-driven phase transitions to form lower-symmetry polymorphs with antiferrodistortive displacement patterns.<sup>34</sup> The prototypical high-temperature

perovskite phase is a cubic structure. As the temperature is reduced, lower-symmetry tetragonal and orthorhombic perovskite phases can be formed through tilting of the BX<sub>6</sub> octahedra.<sup>35,36</sup> Therefore, it is likely that there are transitions to higher symmetry phases at temperatures above ambient for BaZrS<sub>3</sub>. Phase transitions may occur before reaching the elevated temperatures required for BaZrS<sub>3</sub> synthesis (>850 K).<sup>13</sup> If this is the case it follows that samples grown at high temperature may include mixtures of polymorphs, as has been observed for halide perovskites.<sup>37,38</sup> A phase transition within the operating temperature range for thermoelectric generators (400 to 1100 K) is also possible. An understanding of the exact BaZrS<sub>3</sub> perovskite structure is important as even small changes to structure can impact key functional properties including the band gap.<sup>39,40</sup> Anharmonic dynamics are also crucial for quantitative predictions of electron–phonon coupling and related optical properties.

In this work, we use molecular dynamics (MD) to sample the anharmonic free energy surface and simulate the finite-temperature dynamics of the BaZrS<sub>3</sub> perovskite. We accelerate

**Received:** December 9, 2024

**Revised:** February 7, 2025

**Accepted:** February 13, 2025

the calculation of free energies, atomic forces, and stress tensors necessary for MD by constructing a machine learning interatomic potential with training data from density functional theory (DFT) calculations using a hybrid exchange-correlation functional. We apply known group-subgroup relationships to systematically identify which octahedral tilt patterns can be accessed during phase transitions. We identify two phase transitions in BaZrS<sub>3</sub> at 0 Pa: a first-order orthorhombic *Pnma* to tetragonal *I4/mcm* transition at 610 K and a second-order tetragonal *I4/mcm* to cubic *Pm* $\bar{3}$ *m* phase transition at 880 K. We construct a phase diagram for BaZrS<sub>3</sub> across a pressure and temperature range of  $-4$  to 10 GPa and 0 K to 1200 K, respectively. Lastly, we predict the Raman spectra and temperature-dependent XRD patterns, and compare our predictions against published experimental data.

## METHODS

A machine learning interatomic potential was constructed using the neuroevolution potential (NEP) method implemented in the GPUMD package.<sup>41</sup> The ASE and CALORINE packages were used to prepare the training structures, set up MD simulations, and postprocess the results.<sup>42,43</sup> The training set consists of 1187 perovskite structures. This includes cubic, tetragonal, and orthorhombic phases with applied strain or small random displacements, all 15 Glazer-tilt structures,<sup>44,45</sup> and snapshots from NPT MD simulations. The training set also contains 92 Ruddlesden–Popper structures, which will be the subject of a future publication. Symmetry-constrained geometry relaxations as implemented in ASE were performed until the maximal force component was below  $10^{-3}$  eV/Å.<sup>42</sup> DFT calculations were performed using the FHI-AIMS code and the HSE06 exchange-correlation functional.<sup>46,47</sup> The root mean squared training errors were 1.8 meV/atom, 72.2 meV/Å, and 28.9 meV/atom for formation energies, atomic forces, and virials, respectively; see Figure S1 for the loss curves and Figure S2 for the parity plots. Harmonic phonon dispersions were evaluated using the PHONOPY package with  $2 \times 2 \times 2$  supercells and 0.01 Å displacements.<sup>48</sup> For a comparison of the NEP-calculated and DFT-calculated harmonic phonon dispersions see Figures S3–S5.

Heating and cooling simulations with supercells of 40 960 atoms were run in the NPT ensemble in the temperature range of 0 to 1200 K and a pressure range of  $-4$  to 10 GPa using a time step of 1 fs. To identify the symmetry group formed, atomic displacements were projected onto the octahedral-tilt phonon eigenvectors of the cubic structure, as outlined in ref 49. Mode projections amplitudes for the NEP-relaxed and DFT-relaxed structures are given in Tables S2 and S1, respectively. Free energy calculations were carried out using thermodynamic integration (TI) with an Einstein crystal as reference Hamiltonian.<sup>50</sup> To calculate the XRD pattern  $I(\theta)$  the DYNASOR package was used to postprocess NVT MD simulations.<sup>51</sup> For more computational details see the Supporting Information.

In Figure 1a and Figure 1b we plot the harmonic phonon dispersions and crystal structures of BaZrS<sub>3</sub> in the cubic *Pm* $\bar{3}$ *m* phase and experimentally observed *Pnma* phase. The aristotype cubic *Pm* $\bar{3}$ *m* phase is the simplest perovskite form. However, perovskites often adopt lower-symmetry, distorted noncubic phases.<sup>52</sup> Distortions in the cubic perovskite give rise to a wide range of structures which can be classified into three categories: (i) BX<sub>6</sub> octahedral tilting; (ii) distortions of the BX<sub>6</sub> octahedra; and (iii) B-site cation displacements.<sup>53,54</sup>

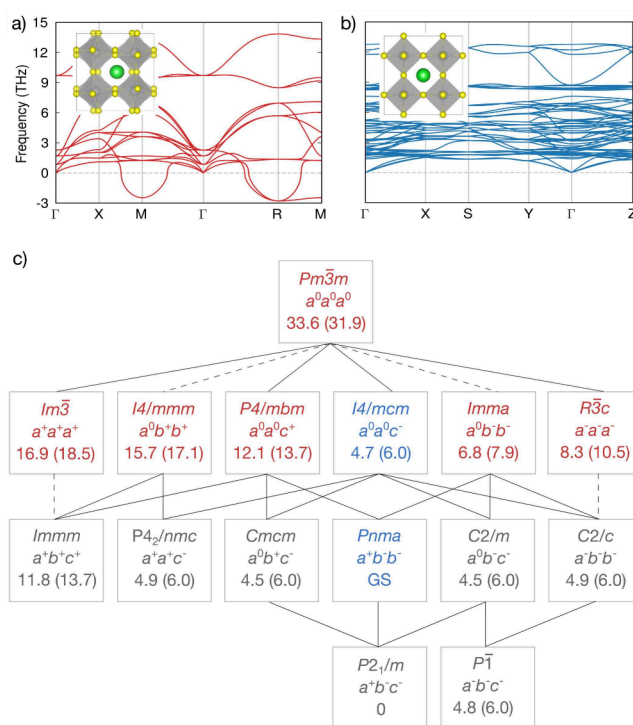


**Figure 1.** DFT-calculated crystal and phonon band structures of the (a) orthorhombic *Pnma* and (b) cubic *Pm* $\bar{3}$ *m* phases. Green, gray, and yellow spheres represent Ba, Zr, and S atoms, respectively. (c) Group-subgroup relationships and 0 K formation energies. The space group, Glazer notation, and formation energy are specified for each phase accessible through octahedral tilting. The formation energies (in meV/atom) with respect to the ground-state (GS) *Pnma* phase obtained from DFT and NEP model calculations (in parentheses) are reported in the bottom rows. Connecting lines indicate group-subgroup relationships. Dashed lines indicate transitions that must be first order according to Landau theory.<sup>45</sup> Red text denotes the presence of phonon modes with an imaginary frequency, indicating dynamic instability at 0 K. Blue text denotes dynamic stability. Gray text denotes that the phase is symmetrically equivalent to a supergroup structure after relaxation. There may still be a small discrepancy in formation energy, which is discussed in the Supporting Information. Figure adapted from Howard and Stokes.<sup>45</sup>

Octahedral tilting leads to 15 possible space groups as identified by Glazer.<sup>44</sup>

BaZrS<sub>3</sub> in the cubic *Pm* $\bar{3}$ *m* phase (*a*<sup>0</sup> *a*<sup>0</sup> *a*<sup>0</sup> in Glazer notation) is dynamically unstable indicating the presence of a lower-symmetry stable structure at 0 K.<sup>55</sup> The imaginary phonon modes at the M point of the Brillouin zone correspond to in-phase (+) tilting of the ZrS<sub>6</sub> octahedra and are described by the irrep M<sub>2</sub><sup>+</sup> (for a unit cell with an origin at the B-site).<sup>56</sup> The imaginary modes at the R point correspond to out-of-phase (−) tilting and have irrep R<sub>5</sub><sup>−</sup>. Both modes are triply degenerate. Distortions along one M-mode and two perpendicular R-modes result in a dynamically stable orthorhombic *Pnma* phase (*a*<sup>+</sup> *b*<sup>−</sup> *b*<sup>−</sup>). The dynamic and energetic stability of the orthorhombic phase at 0 K is in agreement with previous experimental and DFT studies reporting it to be stable at low temperatures.<sup>57–59</sup>

Distortions along linear combinations of the M- and R-modes result in 15 unique space groups. We display the group-subgroup relationships and 0 K formation energies for BaZrS<sub>3</sub> in Figure 1c. As expected, *Pm* $\bar{3}$ *m* is the highest energy phase relative to the *Pnma* ground state. *I4/mcm* is 4.7 meV/atom

above the ground state, indicating that it may form as a higher temperature phase. The comprehensive mapping across all possible structures ensures that we include all octahedral tilt patterns that might be formed at high temperatures in our training data for the machine learning interatomic potential.

Connecting lines in Figure 1c indicate group-subgroup relationships between structures. In Landau theory, this relationship is necessary (but not sufficient) for structures connected through second-order (continuous) phase transitions.<sup>60</sup> Dashed lines indicate that, despite sharing a group-subgroup relationship, the phase transition must be first-order (discontinuous) in Landau theory.<sup>61</sup>

In Figure 2, we plot properties observed and derived from MD simulations spanning 0 to 1200 K and with no applied pressure. When heating the low-temperature *Pnma* structure there are phase transitions at 650 and 880 K. The transition at 650 K is accompanied by a discontinuous and sharp change in lattice parameters (Figure 2a). Two of the lattice parameters become equal, indicating an orthorhombic to tetragonal transition. In contrast, the transition at 880 K is gradual and continuous. All three lattice parameters become equal, indicating a tetragonal-to-cubic transition.

In Figure 2b,c we show projections of the M and R phonon modes on structures sampled from the simulation. From 0 to 650 K one M-mode and two R-modes are active (have a non-zero amplitude). This tilt pattern is described by  $a^+ b^- b^-$  in Glazer notation and corresponds to a structure in the *Pnma* space group (see Figure 1 and the associated discussion). From 650 K to 880, only one R-mode is activated corresponding to the tetragonal *I4/mcm* phase ( $a^0 a^0 c^-$ ). Above 900 K, no modes are activated indicating the existence of a cubic *Pm3m* phase ( $a^0 a^0 a^0$ ).

A sharp discontinuity is observed in energy (Figure 2d) and heat capacity (Figure 2e) at 650 K. The 1 meV/atom energy change is the latent heat associated with a first-order phase transition and is comparable to that observed in other perovskites.<sup>35,36</sup> At 880 K a continuous change in energy is observed, typical of second-order phase transitions, resulting in a broader, less pronounced peak in the heat capacity. We conclude that there is a first-order *Pnma*-to-*I4/mcm* transition at 650 K, and a second-order *I4/mcm*-to-*Pm3m* transition at 880 K. These observations are consistent with the group-subgroup analysis presented in Figure 1. The *Pnma* phase does not share a group-subgroup relationship with *I4/mcm*, necessitating a first-order phase transition. In contrast, is a subgroup of the *Pm3m* phase, so can be accessed through a second-order transition.

In the cooling runs, we start from the high-temperature *Pm3m* structure and reproduce the heating behavior for the second-order transition at 880 K. Significant hysteresis is observed for the first-order phase transition at 650 K as the system cannot overcome the free energy barrier required to form the orthorhombic phase. Due to the stochastic nature of MD simulations, we do recover the orthorhombic phase in some of the cooling runs (Figure S6). Hysteresis in simulations describing a first-order transition has been observed and discussed in previous studies.<sup>35,36,62</sup>

In many materials transitions to new phases can be induced through applied pressure or strain. In Figure 3, we present the BaZrS<sub>3</sub> pressure–temperature phase diagram across −4 to 10 GPa and 0 to 1000 K. Negative pressures correspond to triaxial tensile strain. While this is difficult to realize experimentally, tensile strain in a plane can be produced through coherent

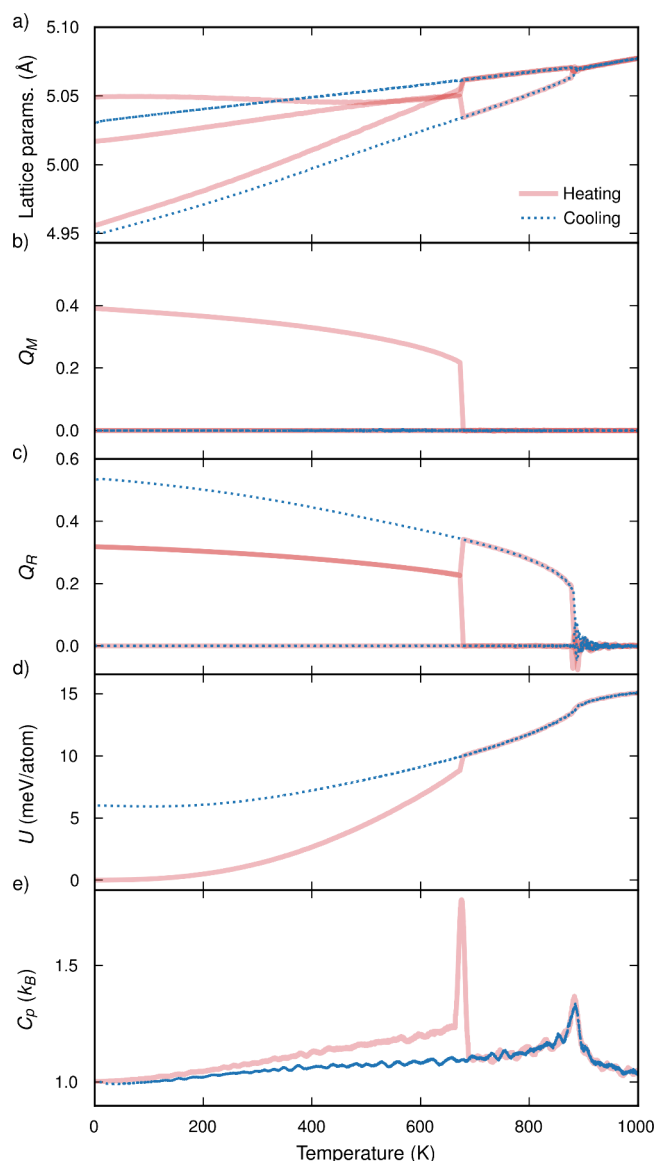


**Figure 2.** Properties of the BaZrS<sub>3</sub> perovskite from cooling (blue) and heating (red) simulations: (a) pseudocubic lattice parameters; (b) M-mode and (c) R-mode amplitudes ( $Q_M$ ,  $Q_R$ ); (d) energies ( $U$ ); (e) heat capacities ( $C_p$ ). Energies are shown relative to the *Pnma* ground-state energy at 0 K with the equipartition energy ( $\frac{3}{2} k_B T$ ) subtracted. The heat capacity is obtained by calculating the numerical derivative of the energy with respect to temperature,  $C_p = dU/dT$ , and is reported per degree of freedom in the system. The simulation time scale is 200 ns. All quantities are averaged over a time period of 0.8 ns.

interface formation with a suitably matched substrate.<sup>63</sup> As such, Figure 3 indicates the range of polymorphs which might be accessed through interface engineering in a device stack. To accurately predict the first-order *Pnma*-to-*I4/mcm* phase transition temperatures we use thermodynamic integration to calculate free energies. This still describes the full anharmonicity of the material but avoids the kinetic limitations of a cooling or heating simulation which must overcome the first-order transition barrier.<sup>36</sup>

The higher symmetry phases are stabilized with increasing temperature or decreasing pressure. This indicates that the ZrS<sub>6</sub> octahedra are relatively rigid, with volume expansion driven through decreased octahedral tilting;<sup>64</sup> see the

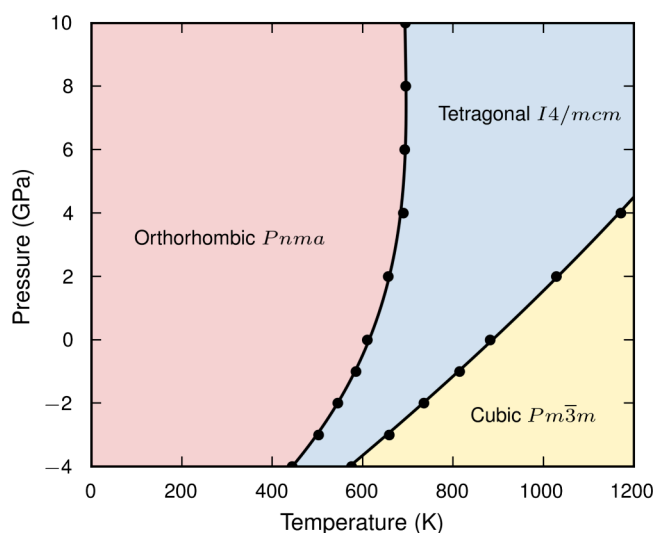


**Figure 3.** Phase diagram of BaZrS<sub>3</sub> as a function of pressure and temperature. To predict the first-order *Pnma*-to-*I4/mcm* phase transition temperatures we use thermodynamic integration to calculate free energies. The second-order *I4/mcm*-to-*Pm* $\bar{3}m$  phase transition temperatures are calculated from heating runs (Figure 2).

discussion on perovskite bond compressibility in the SI. At zero pressure the *Pnma*-to-*I4/mcm* phase transition temperature is 610 K. For comparison, the phase transition temperature in the harmonic approximation is 243 K (Figure S8). Above 4 GPa, the transition temperature saturates at 690 K. Below 400 K there are no structural changes between  $-4$  to 10 GPa. This is in agreement with a previous DFT study at 0 K and Raman measurements across the pressure range 0 to 8.9 GPa.<sup>28,65</sup>

Our simulations show that BaZrS<sub>3</sub> forms in the *Pnma* structure at room temperature. This observation is supported by experimental characterization in ambient conditions and computational predictions at 0 K.<sup>2,19,28,66</sup> A recent computational study predicts that the polar *Pna*2<sub>1</sub> phase is 0.05 meV per formula unit more stable than *Pnma* at 0 K and 0 GPa.<sup>67</sup> This instability has been observed across a variety of oxide perovskites in the orthorhombic *Pnma* phase.<sup>68</sup> For BaZrS<sub>3</sub> the small 0.05 meV energy difference follows small differences in atomic coordinates, with an extremely tight symmetry tolerance of 0.003 Å required to differentiate between the phases.

A multimodal study combining synchrotron XRD, Raman spectroscopy, optical measurements and thermal analysis as a function of temperature identified three polymorphs when BaZrS<sub>3</sub> is heated in air.<sup>32</sup> Rietveld analysis of the synchrotron powder XRD patterns showed the *I4/mcm* phase to be stable above 770 K and the *Pnma* phase to be stable below 570 K. From 570 to 770 K indirect observations suggest that the orthorhombic *Cmcm* space group co-exists as a minority phase. Despite including the *Cmcm* phase in our training data, our simulations do not predict *Cmcm* as a stable intermediate phase. In fact, at 0 K our DFT calculations show that this phase is kinetically unstable and relaxes to the higher symmetry *I4/mcm* phase (Table S1).

In a separate study from Bystrický et al., temperature-dependent XRD data from a non-synchrotron source also indicated an orthorhombic-to-tetragonal phase transition at 770 K.<sup>23,31</sup> Full structure refinements were not presented and the measurements were partially obstructed through oxidation.

According to the analysis of that data above 770 K, the two unique lattice parameters converge,<sup>23</sup> which we also observe while approaching the second-order *I4/mcm*-to-*Pm* $\bar{3}m$  transition in our MD simulation (Figure 2a).

We present a prediction of the temperature-dependent XRD pattern in Figure 4. At high temperature, the characteristic

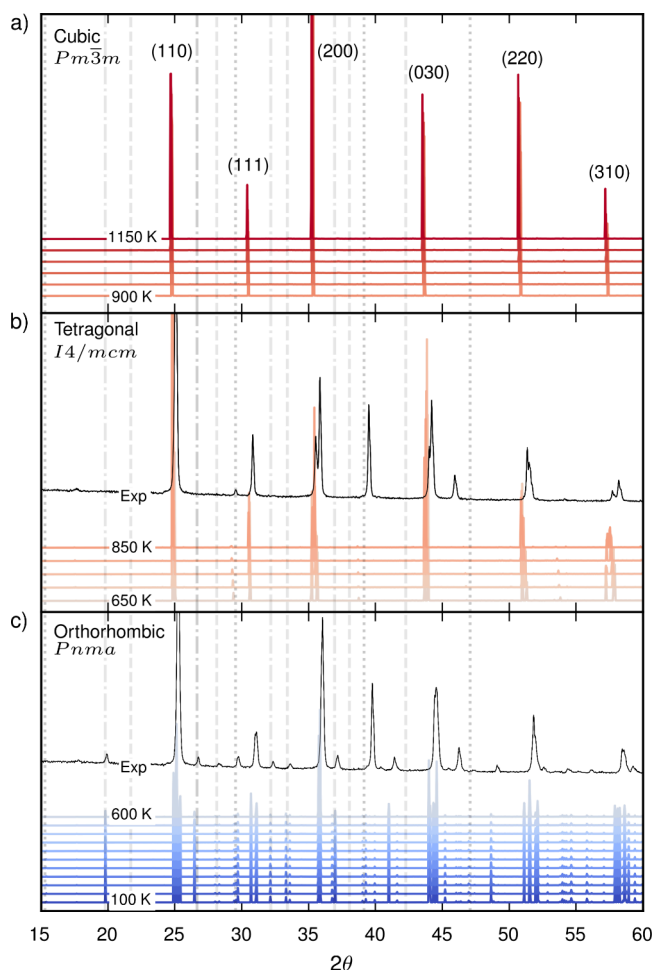


**Figure 4.** X-ray diffraction (XRD) pattern evaluated for three BaZrS<sub>3</sub> polymorphs. The temperature ranges from 100 to 1150 K in intervals of 50 K. All simulations are at 0 Pa. A Cu  $K\alpha$  value of 1.5406 Å was used for the  $q$  to  $\theta$  conversion. Cubic *Pm* $\bar{3}m$  peaks are indexed. Superlattice peaks at half integer planes up to the third Brillouin zone are indicated with vertical lines. The R-, M-, and X-point distortions are represented with dotted, dashed, and dash-dotted lines, respectively. For comparison, Figure S11 displays the static structure factor up to the fifth Brillouin zone. Experimental XRD data for the orthorhombic (303 K) and tetragonal (923 K) phases from ref 31 are plotted in black. The peaks in the experimental data at 39° and 46° are associated with the Pt strip used for heating the sample.

peaks of a cubic perovskite are clearly identified (Figure 4a). Below 900 K, we observe peak splittings of the cubic diffraction lines. From 650 to 900 K the largest splitting corresponds to a  $h00$  reflection (200), and the  $hhh$  reflection (111) remains a singlet, indicating a tetragonal distortion.<sup>54</sup>

Experimental XRD data from Bystrický et al. is displayed in Figure 4b for comparison against our predictions.<sup>31</sup> The structure was refined in the tetragonal space group *I4<sub>1</sub>/acd* which, to the best of our knowledge, has not been previously reported for an ABX<sub>3</sub> perovskite. We find good agreement

between the experimental results and our prediction for the higher-symmetry  $I4/mcm$  phase. R-mode activation produces a doubling of the unit cell along one axis and the appearance of a superlattice peak at a half-integer plane. This can be seen in both the experimental and simulation data at  $2\theta \approx 29^\circ$ .

Above 600 K, an abrupt change is observed due to the first-order phase transition into the orthorhombic phase (Figure 4c). M-point distortions result in the appearance of additional superlattice peaks at  $27^\circ$  and  $33^\circ$  alongside further peak splitting. Superlattice peaks associated with X-mode distortions also appear at  $20^\circ$ ,  $26^\circ$ ,  $32^\circ$  and  $37^\circ$ . The same behavior is observed in the experimental XRD data measured at 303 K.<sup>31</sup> Decomposition of the XRD intensity (Figure S13) shows that some X-point peaks are associated with off-centering of the Ba species. A-site cation off-centering is frequently observed when R-point and M-point distortions operate in tandem.<sup>39</sup>

Transitions between structurally similar perovskite phases are not always discernible in Raman spectra, as the peak splitting can be less than the peak broadening resulting from thermal fluctuations or higher-order scattering.<sup>69–71</sup> The spectral energy densities of the  $I4/mcm$  and  $Pm\bar{3}m$  phases demonstrate that there is considerable phonon broadening at elevated temperatures (Figure S7). While Ye et al. reported that there is no indication of a first-order phase transition between 10 to 875 K,<sup>33</sup> Jaiswal et al. found the number of Raman peaks to decrease with increasing temperature, indicative of a phase transition to a higher-symmetry structure.<sup>32</sup> Our simulated Raman spectra in Figure S9 and Figure S10 demonstrates that there is significant peak overlap between the  $Pnma$  and  $I4/mcm$  phases. Our spectra also reproduces the two most pronounced changes with temperature from Jaiswal et al.: removal of the  $A_g^6$  peak and a significant shift in the  $B_g^6$  peak position.

Experimental characterization of the high-temperature  $Pm\bar{3}m$  phase is hindered by oxidation which leads to the formation of  $BaSO_4$ ,  $ZrO_2$  and  $SO_2$ . Differential scanning calorimetry and thermogravimetric analysis show that  $BaZrS_3$  is stable in air up to 920 K, with complete conversion to the oxidized products at 970 K.<sup>32,66</sup>

In conclusion, chalcogenide perovskites, in particular  $BaZr$ , show great potential for applications in optoelectronic and thermoelectric technologies. However, several aspects of fundamental material behavior, including polymorphic phase transitions, have not previously been explored in detail. In addition, experimental characterisations of the structure through Raman spectroscopy and XRD give conflicting results. We address this problem by developing a machine learning interatomic potential for  $BaZrS_3$  trained on hybrid DFT calculations. This is used to run high-accuracy MD simulations across a wide range of temperatures and pressures.

The structural and thermodynamic properties derived from heating simulations reveal a series of transitions from orthorhombic  $Pnma$ -to-tetragonal  $I4/mcm$ -to-cubic  $Pm\bar{3}m$  with increasing temperature. While this sequence of structures—from the low-symmetry  $Pnma$  phase to the high-symmetry  $Pm\bar{3}m$  phase—is commonly observed in perovskite materials, to the best of our knowledge this is the first report for  $BaZrS_3$ . There is no evidence for additional transitions beyond these before melting. The predicted character of each transition—first-order  $Pnma$ -to- $I4/mcm$  and second-order  $I4/mcm$ -to- $Pm\bar{3}m$ —is in agreement with those allowed by group-subgroup relationships.

Both phase transitions occur above 600 K, which agrees with experimental characterization showing  $BaZrS_3$  is stable in the orthorhombic  $Pnma$  phase at ambient temperature and pressure. In addition, the calculated Raman spectra and temperature-dependent XRD patterns align well with experimental data, supporting our prediction of an orthorhombic-to-tetragonal phase transition and validating our overall approach. The second-order transition at 880 K is more difficult to characterize due to the concurrent high-temperature oxidation processes; further experimental studies in an inert atmosphere are required for confirmation.

It is possible that  $BaZrS_3$  samples grown at high temperature may include mixtures of polymorphs. Future work might more fully consider polymorph mixing, alongside the impact of octahedral tilting on the thermal and optoelectronic properties of  $BaZrS_3$ . We note that the formation of ternary Ruddlesden–Popper phases  $Ba_{n+1}Zr_nS_{3n+1}$  has been considered elsewhere in the literature.<sup>30,72,73</sup> When formed these are likely to have a greater impact on material properties through disruption of the 3D octahedral framework.

## ■ ASSOCIATED CONTENT

### Data Availability Statement

The NEP models generated in this study are openly available via Zenodo at <https://dx.doi.org/10.5281/zenodo.14229468>. The DFT output data has been uploaded to the NOMAD repository and is available at <https://dx.doi.org/10.17172/NOMAD/2024.11.25-2>. A separate repository is also hosted at [https://github.com/NU-CEM/2024\\_BaZrS3\\_Phase\\_Transitions](https://github.com/NU-CEM/2024_BaZrS3_Phase_Transitions) with Python code available to reproduce the figures and analysis.

### Supporting Information

The Supporting Information is available free of charge at <https://pubs.acs.org/doi/10.1021/acs.jpcllett.4c03517>.

Methods and NEP model validation, phonon mode projections for the Glazer tilt structures, results from a cooling run at  $-1$  GPa, temperature-dependent phonon dispersions from molecular dynamics, harmonic free energies and Raman spectra, a discussion on perovskite bond compressibility, and temperature-dependent static structure factors (PDF)

Transparent Peer Review report available (PDF)

## ■ AUTHOR INFORMATION

### Corresponding Author

Lucy Whalley – Department of Mathematics, Physics and Electrical Engineering, Northumbria University, Newcastle upon Tyne NE1 8QH, United Kingdom; [orcid.org/0000-0002-2992-9871](https://orcid.org/0000-0002-2992-9871); Email: [l.whalley@northumbria.ac.uk](mailto:l.whalley@northumbria.ac.uk)

### Authors

Prakriti Kayastha – Department of Mathematics, Physics and Electrical Engineering, Northumbria University, Newcastle upon Tyne NE1 8QH, United Kingdom

Erik Fransson – Department of Physics, Chalmers University of Technology, SE-41296 Gothenburg, Sweden; [orcid.org/0000-0001-5262-3339](https://orcid.org/0000-0001-5262-3339)

Paul Erhart – Department of Physics, Chalmers University of Technology, SE-41296 Gothenburg, Sweden; [orcid.org/0000-0002-2516-6061](https://orcid.org/0000-0002-2516-6061)

Complete contact information is available at: <https://pubs.acs.org/doi/10.1021/acs.jpcllett.4c03517>

## Notes

The authors declare no competing financial interest.

## ACKNOWLEDGMENTS

P.K. is grateful for funding through the Turing Scheme, which facilitated a research visit to Chalmers University of Technology. P.K. also acknowledges support from the UK Engineering and Physical Sciences Research Council (EPSRC) CDT in the Renewable Energy Northeast Universities (ReNU) for funding through EPSRC Grant EP/S023836/1. This work used the Oswald High-Performance Computing Facility operated by Northumbria University (UK). Via our membership in the UK's HEC Materials Chemistry Consortium, which is funded by EPSRC (EP/X035859), this work used the ARCHER2 UK National Supercomputing Service. We are grateful to the UK Materials and Molecular Modelling Hub for computational resources, which is partially funded by EPSRC (EP/T022213/1, EP/W032260/1, and EP/P020194/1). This work has also been supported by the Swedish Research Council (Nos. 2020-04935 and 2021-05072) and the Chalmers Initiative for Advancement of Neutron and Synchrotron Techniques. Some of the computations were enabled by resources provided by the National Academic Infrastructure for Supercomputing in Sweden (NAISS) at C3SE, partially funded by the Swedish Research Council through grant agreement no. 2022-06725, as well as the Berzelius resource provided by the Knut and Alice Wallenberg Foundation at NSC. We thank Fredrik Eriksson, Kostiantyn Sopiha, and Florian Knoop for discussion related to this study. We thank Milan Sýkora and team for sharing the experimental X-ray diffraction data displayed in Figure 4.

## REFERENCES

- (1) Sun, Y.-Y.; Agiorgousis, M. L.; Zhang, P.; Zhang, S. Chalcogenide perovskites for photovoltaics. *Nano Lett.* **2015**, *15*, 581–585.
- (2) Sopiha, K. V.; Comparotto, C.; Márquez, J. A.; Scragg, J. J. Chalcogenide perovskites: tantalizing prospects, challenging materials. *Adv. Opt. Mater.* **2022**, *10*, 2101704.
- (3) Tiwari, D.; Hutter, O. S.; Longo, G. Chalcogenide perovskites for photovoltaics: current status and prospects. *J. Phys.: Energy* **2021**, *3*, No. 034010.
- (4) Jaramillo, R.; Ravichandran, J. In praise and in search of highly-polarizable semiconductors: Technological promise and discovery strategies. *APL Mater.* **2019**, *7*, 100902.
- (5) Choi, J. W.; Shin, B.; Gorai, P.; Hoyer, R. L. Z.; Palgrave, R. Emerging Earth-Abundant Solar Absorbers. *ACS Energy Letters* **2022**, *7*, 1553–1557.
- (6) Nishigaki, Y.; Nagai, T.; Nishiwaki, M.; Aizawa, T.; Kozawa, M.; Hanzawa, K.; Kato, Y.; Sai, H.; Hiramatsu, H.; Hosono, H.; et al. Extraordinary strong band-edge absorption in distorted chalcogenide perovskites. *Solar Rrl* **2020**, *4*, 1900555.
- (7) Ravi, V. K.; Yu, S. H.; Rajput, P. K.; Nayak, C.; Bhattacharyya, D.; Chung, D. S.; Nag, A. Colloidal BaZrS<sub>3</sub> chalcogenide perovskite nanocrystals for thin film device fabrication. *Nanoscale* **2021**, *13*, 1616–1623.
- (8) Wu, X.; Gao, W.; Chai, J.; Ming, C.; Chen, M.; Zeng, H.; Zhang, P.; Zhang, S.; Sun, Y.-Y. Defect tolerance in chalcogenide perovskite photovoltaic material BaZrS<sub>3</sub>. *Science China Materials* **2021**, *64*, 2976–2986.
- (9) Yuan, Z.; Dahliah, D.; Claes, R.; Pike, A.; Fenning, D. P.; Rignanese, G.-M.; Hautier, G. Assessing carrier mobility, dopability, and defect tolerance in the chalcogenide perovskite BaZrS<sub>3</sub>. *arXiv* **2024**, 2405.09793.
- (10) Yu, Z.; Wei, X.; Zheng, Y.; Hui, H.; Bian, M.; Dhole, S.; Seo, J.-H.; Sun, Y.-Y.; Jia, Q.; Zhang, S.; et al. Chalcogenide perovskite BaZrS<sub>3</sub> thin-film electronic and optoelectronic devices by low temperature processing. *Nano Energy* **2021**, *85*, 105959.
- (11) Yang, R.; Jess, A. D.; Fai, C.; Hages, C. J. Low-temperature, solution-based synthesis of luminescent chalcogenide perovskite BaZrS<sub>3</sub> nanoparticles. *J. Am. Chem. Soc.* **2022**, *144*, 15928–15931.
- (12) Pradhan, A. A.; Uible, M. C.; Agarwal, S.; Turnley, J. W.; Khandelwal, S.; Peterson, J. M.; Blach, D. D.; Swope, R. N.; Huang, L.; Bart, S. C.; et al. Synthesis of BaZrS<sub>3</sub> and BaHfS<sub>3</sub> chalcogenide perovskite films using single-phase molecular precursors at moderate temperatures. *Angew. Chem.* **2023**, *135*, No. e202301049.
- (13) Comparotto, C.; Strom, P.; Donzel-Gargand, O.; Kubart, T.; Scragg, J. J. Synthesis of BaZrS<sub>3</sub> perovskite thin films at a moderate temperature on conductive substrates. *ACS Applied Energy Materials* **2022**, *5*, 6335–6343.
- (14) Turnley, J. W.; Vincent, K. C.; Pradhan, A. A.; Panicker, I.; Swope, R.; Uible, M. C.; Bart, S. C.; Agrawal, R. Solution deposition for chalcogenide perovskites: a low-temperature route to BaMS<sub>3</sub> materials (M= Ti, Zr, Hf). *J. Am. Chem. Soc.* **2022**, *144*, 18234–18239.
- (15) Sharma, S.; Ward, Z.; Bhimani, K.; Li, K.; Lakhnot, A.; Jain, R.; Shi, S.-F.; Terrones, H.; Koratkar, N. Bandgap tuning in BaZrS<sub>3</sub> perovskite thin films. *ACS Applied Electronic Materials* **2021**, *3*, 3306–3312.
- (16) Sadeghi, I.; Van Sambeek, J.; Simonian, T.; Xu, M.; Ye, K.; Cai, T.; Nicolosi, V.; LeBeau, J. M.; Jaramillo, R. Expanding the perovskite periodic table to include chalcogenide alloys with tunable band gap spanning 1.5–1.9 eV. *Adv. Funct. Mater.* **2023**, *33*, 2304575.
- (17) Meng, W.; Saparov, B.; Hong, F.; Wang, J.; Mitzi, D. B.; Yan, Y. Alloying and defect control within chalcogenide perovskites for optimized photovoltaic application. *Chem. Mater.* **2016**, *28*, 821–829.
- (18) Dallas, P.; Gkini, K.; Kaltzoglou, A.; Givalou, L.; Konstantakou, M.; Orfanoudakis, S.; Boukos, N.; Sakellis, E.; Tsiapas, P.; Kalafatis, A.; et al. Exploring the potential of powder-to-film processing for proof-of-concept BaZrS<sub>3</sub> perovskite solar cells. *Materials Today Communications* **2024**, *39*, 108608.
- (19) Agarwal, S.; Vincent, K. C.; Agrawal, R. From synthesis to application: a review of BaZrS<sub>3</sub> chalcogenide perovskites. *Nanoscale* **2025**, DOI: 10.1039/D4NR03880K.
- (20) Osei-Agyemang, E.; Koratkar, N.; Balasubramanian, G. Examining the electron transport in chalcogenide perovskite BaZrS<sub>3</sub>. *Journal of Materials Chemistry C* **2021**, *9*, 3892–3900.
- (21) Osei-Agyemang, E.; Balasubramanian, G. Understanding the extremely poor lattice thermal transport in chalcogenide perovskite BaZrS<sub>3</sub>. *ACS Applied Energy Materials* **2020**, *3*, 1139–1144.
- (22) Yang, Z.; Han, Y.; Liang, Y.; Shen, W.; Zhang, Z.; Fang, C.; Wang, Q.; Wan, B.; Chen, L.; Zhang, Y.; et al. Chalcogenide perovskite BaZrS<sub>3</sub> bulks for thermoelectric conversion with ultra-high carrier mobility and low thermal conductivity. *Acta Mater.* **2024**, *276*, 120156.
- (23) Jaykhedkar, N.; Bystrický, R.; Sýkora, M.; Bučko, T. How the temperature and composition govern the structure and band gap of Zr-based chalcogenide perovskites: Insights from ML accelerated AIMD. *Inorg. Chem.* **2023**, *62*, 12480–12492.
- (24) Comparotto, C.; Davydova, A.; Ericson, T.; Riekehr, L.; Moro, M. V.; Kubart, T.; Scragg, J. Chalcogenide perovskite BaZrS<sub>3</sub>: thin film growth by sputtering and rapid thermal processing. *ACS Applied Energy Materials* **2020**, *3*, 2762–2770.
- (25) Xu, J.; Fan, Y.; Tian, W.; Ye, L.; Zhang, Y.; Tian, Y.; Han, Y.; Shi, Z. Enhancing the optical absorption of chalcogenide perovskite BaZrS<sub>3</sub> by optimizing the synthesis and post-processing conditions. *Solid State Chem.* **2022**, *307*, 122872.
- (26) Niu, S.; Zhao, B.; Ye, K.; Bianco, E.; Zhou, J.; McConney, M. E.; Settens, C.; Haiges, R.; Jaramillo, R.; Ravichandran, J. Crystal growth and structural analysis of perovskite chalcogenide BaZrS<sub>3</sub> and Ruddlesden–Popper phase Ba<sub>3</sub>Zr<sub>2</sub>S<sub>7</sub>. *J. Mater. Res.* **2019**, *34*, 3819–3826.
- (27) Mukherjee, S.; Riva, S.; Comparotto, C.; Johansson, F. O.; Man, G. J.; Phuyal, D.; Simonov, K. A.; Just, J.; Klementiev, K.; Butorin, S. M.; et al. Interplay between growth mechanism, materials

chemistry, and band gap characteristics in sputtered thin films of chalcogenide perovskite BaZrS<sub>3</sub>. *ACS Applied Energy Materials* **2023**, *6*, 11642–11653.

(28) Gross, N.; Sun, Y.-Y.; Perera, S.; Hui, H.; Wei, X.; Zhang, S.; Zeng, H.; Weinstein, B. Stability and band-gap tuning of the chalcogenide perovskite BaZrS<sub>3</sub> in Raman and optical investigations at high pressures. *Physical Review Applied* **2017**, *8*, No. 044014.

(29) Filippone, S.; Zhao, B.; Niu, S.; Koocher, N. Z.; Silevitch, D.; Fina, I.; Rondinelli, J. M.; Ravichandran, J.; Jaramillo, R. Discovery of highly polarizable semiconductors BaZrS<sub>3</sub> and Ba<sub>3</sub>Zr<sub>2</sub>S<sub>7</sub>. *Physical Review Materials* **2020**, *4*, No. 091601.

(30) Kayastha, P.; Tiwari, D.; Holland, A.; Hutter, O. S.; Durose, K.; Whalley, L. D.; Longo, G. High-Temperature Equilibrium of 3D and 2D Chalcogenide Perovskites. *Solar RRL* **2023**, *7*, 2201078.

(31) Bystrický, R.; Tiwari, S. K.; Hutár, P.; Sýkora, M. Thermal Stability of Chalcogenide Perovskites. *Inorg. Chem.* **2024**, *63*, 12826–12838.

(32) Jaiswal, A.; Sakharov, K. A.; Lekina, Y.; Kamonsuangkasem, K.; Tomm, Y.; Wei, F.; White, T. J. High-Temperature Polymorphism and Band-Gap Evolution in BaZrS<sub>3</sub>. *Inorg. Chem.* **2024**, *63*, 24157–24166.

(33) Ye, K.; Menahem, M.; Salzillo, T.; Knoop, F.; Zhao, B.; Niu, S.; Hellman, O.; Ravichandran, J.; Jaramillo, R.; Yaffe, O. Differing vibrational properties of halide and chalcogenide perovskite semiconductors and impact on optoelectronic performance. *Physical Review Materials* **2024**, *8*, No. 085402.

(34) Redfern, S. A. High-temperature structural phase transitions in perovskite. *J. Phys.: Condens. Matter* **1996**, *8*, 8267.

(35) Fransson, E.; Wiktor, J.; Erhart, P. Phase transitions in inorganic halide perovskites from machine-learned potentials. *J. Phys. Chem. C* **2023**, *127*, 13773–13781.

(36) Fransson, E.; Rahm, J. M.; Wiktor, J.; Erhart, P. Revealing the Free Energy Landscape of Halide Perovskites: Metastability and Transition Characters in CsPbBr<sub>3</sub> and MAPbI<sub>3</sub>. *Chem. Mater.* **2023**, *35*, 8229–8238.

(37) Dubajic, M.; et al. Dynamic Nanodomains Dictate Macroscopic Properties in Lead Halide Perovskites. *arXiv* 2023; DOI: 10.48550/arxiv.2404.14598.

(38) Weadock, N. J.; et al. The nature of dynamic local order in CH<sub>3</sub>NH<sub>3</sub>PbI<sub>3</sub> and CH<sub>3</sub>NH<sub>3</sub>PbBr<sub>3</sub>. *Joule* **2023**, *7*, 1051–1066.

(39) Glazer, A. M. Simple ways of determining perovskite structures. *Acta Crystallogr., Sect. A* **1975**, *31*, 756–762.

(40) Linaburg, M. R.; McClure, E. T.; Majher, J. D.; Woodward, P. M. Cs<sub>1-x</sub>RbxPbCl<sub>3</sub> and Cs<sub>1-x</sub>RbxPbBr<sub>3</sub> Solid Solutions: Understanding Octahedral Tilting in Lead Halide Perovskites. *Chem. Mater.* **2017**, *29*, 3507–3514.

(41) Fan, Z.; et al. GPUMD: A package for constructing accurate machine-learned potentials and performing highly efficient atomistic simulations. *J. Chem. Phys.* **2022**, *157*, 114801.

(42) Hjorth Larsen, A.; et al. The atomic simulation environment - a Python library for working with atoms. *J. Phys.: Condens. Matter* **2017**, *29*, 273002.

(43) Lindgren, E.; Rahm, M.; Fransson, E.; Eriksson, F.; Österbacka, N.; Fan, Z.; Erhart, P. calorine: A Python package for constructing and sampling neuroevolution potential models. *Journal of Open Source Software* **2024**, *9*, 6264.

(44) Glazer, A. M. The classification of tilted octahedra in perovskites. *Acta Crystallographica Section B: Structural Crystallography and Crystal Chemistry* **1972**, *28*, 3384–3392.

(45) Howard, C. J.; Stokes, H. T. Group-theoretical analysis of octahedral tilting in perovskites. *Acta Crystallographica Section B: Structural Science* **1998**, *54*, 782–789.

(46) Blum, V.; Gehrke, R.; Hanke, F.; Havu, P.; Havu, V.; Ren, X.; Reuter, K.; Scheffler, M. Ab initio molecular simulations with numeric atom-centered orbitals. *Comput. Phys. Commun.* **2009**, *180*, 2175–2196.

(47) Krukau, A. V.; Vydrov, O. A.; Izmaylov, A. F.; Scuseria, G. E. Influence of the exchange screening parameter on the performance of screened hybrid functionals. *J. Chem. Phys.* **2006**, *125*, 224106.

(48) Togo, A. First-principles phonon calculations with phonopy and phono3py. *J. Phys. Soc. Jpn.* **2023**, *92*, No. 012001.

(49) Fransson, E.; Rosander, P.; Eriksson, F.; Rahm, J. M.; Tadano, T.; Erhart, P. Limits of the phonon quasi-particle picture at the cubic-to-tetragonal phase transition in halide perovskites. *Communications Physics* **2023**, *6*, 173.

(50) Frenkel, D.; Ladd, A. J. C. New Monte Carlo Method to Compute the Free Energy of Arbitrary Solids. Application to the Fcc and Hcp Phases of Hard Spheres. *J. Chem. Phys.* **1984**, *81*, 3188–3193.

(51) Fransson, E.; Slabanja, M.; Erhart, P.; Wahnström, G. dynasor - A Tool for Extracting Dynamical Structure Factors and Current Correlation Functions from Molecular Dynamics Simulations. *Advanced Theory and Simulations* **2021**, *4*, 2000240.

(52) Tilley, R. J. *Perovskites: structure-property relationships*; John Wiley & Sons, 2016.

(53) Lufaso, M. W.; Woodward, P. M. Jahn–Teller distortions, cation ordering and octahedral tilting in perovskites. *Acta Crystallographica Section B: Structural Science* **2004**, *60*, 10–20.

(54) Howard, C. J.; Stokes, H. T. Structures and phase transitions in perovskites—a group-theoretical approach. *Acta Crystallographica Section A: Foundations of Crystallography* **2005**, *61*, 93–111.

(55) Pallikara, I.; Kayastha, P.; Skelton, J. M.; Whalley, L. D. The physical significance of imaginary phonon modes in crystals. *Electronic Structure* **2022**, *4*, No. 033002.

(56) Glazer, A. M. *A Journey into Reciprocal Space*, 2nd ed.; IOP Publishing, 2021.

(57) Lelieveld, R.; Ijdo, D. Sulphides with the GdFeO<sub>3</sub> structure. *Acta Crystallographica Section B: Structural Crystallography and Crystal Chemistry* **1980**, *36*, 2223–2226.

(58) Okai, B.; Takahashi, K.; Saeki, M.; Yoshimoto, J. Preparation and crystal structures of some complex sulphides at high pressures. *Materials research bulletin* **1988**, *23*, 1575–1584.

(59) Perera, S.; Hui, H.; Zhao, C.; Xue, H.; Sun, F.; Deng, C.; Gross, N.; Milleville, C.; Xu, X.; Watson, D. F.; et al. Chalcogenide perovskites—an emerging class of ionic semiconductors. *Nano Energy* **2016**, *22*, 129–135.

(60) Landau, L. D.; Lifshitz, E. M. *Statistical Physics*; Elsevier, 2013; Vol. 5.

(61) Stokes, H. T.; Hatch, D. M. Group-subgroup structural phase transitions: A comparison with existing tables. *Phys. Rev. B* **1984**, *30*, 4962.

(62) Zhong, W.; Vanderbilt, D.; Rabe, K. First-principles theory of ferroelectric phase transitions for perovskites: The case of BaTiO<sub>3</sub>. *Phys. Rev. B* **1995**, *52*, 6301.

(63) Choi, M.-J.; Lee, J.-W.; Jang, H. W. Strain Engineering in Perovskites: Mutual Insight on Oxides and Halides. *Adv. Mater.* **2024**, *36*, 2308827.

(64) Angel, R. J.; Zhao, J.; Ross, N. L. General rules for predicting phase transitions in perovskites due to octahedral tilting. *Physical review letters* **2005**, *95*, No. 025503.

(65) Rong, Z.; Zhi, C.; Jun, C. Ab initio calculation of mechanical, electronic and optical characteristics of chalcogenide perovskite BaZrS<sub>3</sub> at high pressures. *Acta Crystallographica Section C* **2022**, *78*, 570–577.

(66) Niu, S.; Milam-Guerrero, J.; Zhou, Y.; Ye, K.; Zhao, B.; Melot, B. C.; Ravichandran, J. Thermal stability study of transition metal perovskite sulfides. *J. Mater. Res.* **2018**, *33*, 4135–4143.

(67) Yaghoubi, A.; Patterson, R.; Hao, X. Exotic ferroelectricity in strained BaZrS<sub>3</sub> chalcogenide perovskite for photovoltaics. *Communications Materials* **2024**, *5*, 262.

(68) Scott, C. A. M.; Bristowe, N. C. Universal Polar Instability in Highly Orthorhombic Perovskites. *J. Am. Chem. Soc.* **2024**, *146*, 29735–29741 PMID: 39411855.

(69) Cohen, A.; Brenner, T. M.; Klarbring, J.; Sharma, R.; Fabini, D. H.; Korobko, R.; Nayak, P. K.; Hellman, O.; Yaffe, O. Diverging Expressions of Anharmonicity in Halide Perovskites. *Adv. Mater.* **2022**, *34*, 2107932.

(70) Menahem, M.; Benshalom, N.; Asher, M.; Aharon, S.; Korobko, R.; Hellman, O.; Yaffe, O. Disorder origin of Raman scattering in perovskite single crystals. *Physical Review Materials* **2023**, *7*, No. 044602.

(71) Rosander, P.; Fransson, E.; Österbacka, N.; Erhart, P.; Wahnström, G. Untangling the Raman spectrum of cubic and tetragonal BaZrO<sub>3</sub>. *arXiv 2409.16161* 2024.

(72) Kayastha, P.; Longo, G.; Whalley, L. D. A First-Principles Thermodynamic Model for the Ba–Zr–S System in Equilibrium with Sulfur Vapor. *ACS Applied Energy Materials* **2024**, *7*, 11326–11333.

(73) Pradhan, A. A.; Agarwal, S.; Vincent, K. C.; Hayes, D. C.; Peterson, J. M.; Turnley, J. W.; Spilker, R. M.; Uible, M. C.; Bart, S. C.; Huang, L.; Kissinger, K.; Agrawal, R. Emergence of Ruddlesden–Popper phases and other pitfalls for moderate temperature solution deposited chalcogenide perovskites. *Mater. Chem. Front.* **2024**, *8*, 3358–3372.

## Supporting Information:

### Octahedral tilt-driven phase transitions in BaZrS<sub>3</sub> chalcogenide perovskite

Prakriti Kayastha<sup>1</sup>, Erik Fransson<sup>2</sup>, Paul Erhart<sup>2</sup>, and Lucy Whalley<sup>1</sup>

<sup>1</sup> *Department of Physics, Chalmers University of Technology, SE-41296, Gothenburg, Sweden*

<sup>1</sup> *Department of Mathematics, Physics and Electrical Engineering, Northumbria University, Newcastle upon Tyne, NE1 8QH, United Kingdom*

February 7, 2025

## Contents

<b>Methods</b>	<b>2</b>
Density Functional Theory calculations . . . . .	2
Molecular Dynamics . . . . .	2
<b>NEP model validation</b>	<b>4</b>
Comparison of phonon dispersion predicted from DFT and NEP . . . . .	5
<b>Mode projections for Glazer tilt structures</b>	<b>6</b>
<b>Recovery of the orthorhombic phase during cooling at <math>-1</math> GPa</b>	<b>7</b>
<b>Finite-temperature phonons from molecular dynamics</b>	<b>8</b>
<b>Phase transition temperature using the harmonic approximation</b>	<b>9</b>
<b>Perovskite bond compressibility</b>	<b>10</b>
<b>Harmonic Raman spectra</b>	<b>11</b>
<b>Static structure factor</b>	<b>13</b>
<b>Partial static structure factors and X-ray diffraction scattering intensities</b>	<b>15</b>
<b>Supplemental References</b>	<b>17</b>

# Methods

We constructed neuroevolution potential (NEP) models by employing the iterative strategy outlined in Ref. 1. The GPUMD package in version 3.9.4<sup>2-4</sup> was used to build the NEP model and run the molecular dynamics (MD) simulations. The ASE<sup>5</sup> and CALORINE<sup>6</sup> packages were used to prepare the training structures, set up MD simulations and post-process the results.

The initial training set contains strained primitive structures and rattled supercells of the cubic ( $Pm\bar{3}m$ ), tetragonal ( $I4/mcm$ ) and orthorhombic ( $Pnma$ ) perovskite phases, alongside structures corresponding to each of the 15 unique perovskite tilt patterns as specified by Glazer citeglazer1972classification. Random displacements were generated using the HIPHIVE package<sup>7</sup>. The training set also contains 92 Ruddlesden-Popper structures, which will be the subject of a future publication.

The initial model was trained using density functional theory (DFT) data generated with the PBEsol exchange-correlation functional<sup>8</sup>. For each structure in the training set, we calculated the formation energy (relative to the elemental phases), stress tensor and atomic force. This model was then used to run MD simulations in the NPT ensemble, over a temperature and pressure range of 0 K to 1200 K and  $-5$  GPa to 20 GPa respectively, with varying supercell sizes, containing between 20 and 500 atoms. Snapshots from the MD simulations were randomly selected and added to the training set, after which the model was retrained.

Finally, a higher accuracy training set was generated using DFT with the hybrid functional HSE06<sup>9</sup>. Here we carried out single-point calculations on all 1187 training structures generated during the construction of the PBEsol-based model. Stress tensors for structures containing more than 60 atoms were not evaluated as the memory requirements for these calculations were prohibitively large. A comparison of models at the PBEsol level of theory shows that using a sub-set of stress tensors does not impact the predicted phase transition temperature or other properties of interest.

## Density Functional Theory calculations

The training data for each NEP model was generated using DFT calculations to evaluate the formation energies (relative to elemental phases), stress tensors and forces. These calculations were performed using the all-electron numeric atom-centered orbital code FHI-aims<sup>10</sup>. FHI-vibes<sup>11</sup> was used for pre and post-processing of DFT data. All DFT calculations used the *light* basis set and a Monkhorst-Pack  $k$ -point mesh with a minimum  $k$ -spacing of  $0.2/\text{\AA}$ . For single-point calculations, the charge density was converged to an accuracy of  $10^{-6}$ , forces to  $10^{-5}$  eV/ $\text{\AA}$  and stresses to  $10^{-4}$  eV/ $\text{\AA}^3$ . Geometry relaxations were carried out using the symmetry-constrained relaxation scheme as implemented in ASE<sup>5</sup>, until the maximal force component was below  $10^{-3}$  eV/ $\text{\AA}$ .

Harmonic phonon dispersions at 0 K and Helmholtz free energies were evaluated using the PHONOPY package<sup>12</sup> with a  $2 \times 2 \times 2$  supercell and a  $0.01 \text{\AA}$  displacement distance.

## Molecular Dynamics

MD simulations were carried out using the GPUMD software<sup>13</sup> with a timestep of 1 fs. The ASE<sup>5</sup> and calorine<sup>6</sup> packages were used to set up the MD simulations and post-process the results. Heating and cooling simulations were run in the NPT ensemble between 0 K to 1200 K for 200 ns using a supercell consisting of about 40 960 atoms. The potential energy and lattice parameters were recorded every 100 fs to discern phase transitions.

Free energy calculations were carried out via thermodynamic integration (TI) using an Einstein crystal as reference Hamiltonian (also referred to as the Frenkel-Ladd method<sup>14</sup>) as outlined in Ref. 15. The free energy of the system described by the NEP,  $F_{\text{NEP}}$ , is obtained from

$$F_{\text{NEP}} - F_{\text{Ein}} = \int_0^1 \left\langle \frac{dH(\lambda)}{d\lambda} \right\rangle_H d\lambda, \tag{S1}$$

where the integration is carried out over the Kirkwood coupling parameter  $\lambda$ <sup>16</sup>,  $F_{\text{Ein}}$  is the analytically known classical free energy of an Einstein crystal, and the Hamiltonian is  $H(\lambda) = (1 - \lambda) H_{\text{Ein}} + \lambda H_{\text{NEP}}$ , as implemented in GPUMD. Here, the ensemble average  $\langle \dots \rangle_H$  is sampled using the Hamiltonian  $H(\lambda)$ . The Gibbs free energy can then be obtained by  $G = F + PV$ . TI simulations were

run for 0.05 ns using a spring constant of  $4 \text{ eV}/\text{\AA}^2$  using a supercell consisting of 23 040 atoms. These simulations were run in the NVT ensemble with lattice parameters obtained from NPT simulations.

The static structure factor,  $S(\mathbf{q})$ , is calculated from NVT simulations using the DYNASOR package<sup>17</sup> as

$$S(\mathbf{q}) = \frac{1}{N} \left\langle \sum_i^N \sum_j^N \exp[i\mathbf{q} \cdot (\mathbf{r}_i(t) - \mathbf{r}_j(t))] \right\rangle, \quad (\text{S2})$$

where  $\mathbf{r}_i(t)$  is the position of atom  $i$  at time  $t$  and the sums run over all atoms. To obtain the intensity measured in an X-ray experiment,  $I(q)$ , one must include the X-ray form factors as

$$I(q) = \frac{1}{N} \left\langle \sum_i^N \sum_j^N f_i(q) f_j(q) \exp[i\mathbf{q} \cdot (\mathbf{r}_i(t) - \mathbf{r}_j(t))] \right\rangle, \quad (\text{S3})$$

where  $f_i(q)$  is the q-dependent X-ray form factors, here taken from Ref. 18. The partial structure factors and intensities can be obtained by considering only specific atom types in the sums, see Ref. 17. Lastly, we apply Bragg's law to convert the structure factor and intensity from q-space to  $\theta$ -space:

$$\frac{\sin(\theta)}{\lambda} = n \frac{q}{4\pi} \quad (\text{S4})$$

where  $\lambda$  is the wavelength of the incident X-ray beam used in experiment.

We employ phonon mode projection to analyze and classify both relaxed structures and snapshots from MD simulations as done in Ref. 19. The atomic displacements  $\mathbf{u}$  can be projected on a mode  $\lambda$ , with the supercell eigenvector  $\mathbf{e}_\lambda$ , via

$$Q_\lambda = \mathbf{u} \cdot \mathbf{e}_\lambda$$

Here, the phonon supercell eigenvector of the  $R$  and  $M$  tilt modes are obtained with PHONOPY<sup>20</sup>, and symmetrized such that each of the three degenerate modes corresponds to tilting around the x, y, and z direction respectively.

# NEP model validation

Our final training set consists of 1187 structures. Energies, forces, and stress tensors are evaluated using the HSE06 functional. Energies and forces are evaluated for all structures. However, due to large memory requirements, to evaluate stress tensors are only evaluated for structures with less than 60 atoms in the unit cell. Energy and force errors are reported for the entire training set of 1187 structures. Virial and stress errors are only reported for structures where the DFT stress tensors were evaluated.

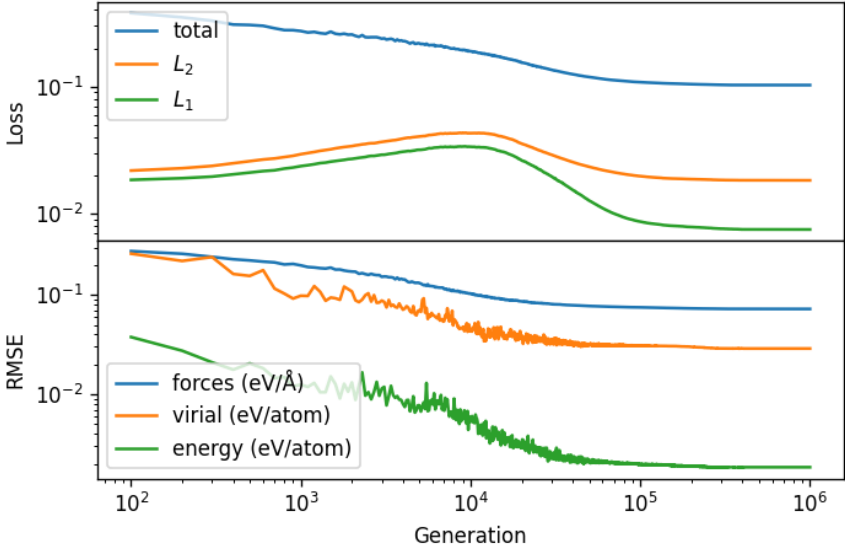


Figure S1: Loss curves for the HSE06 model

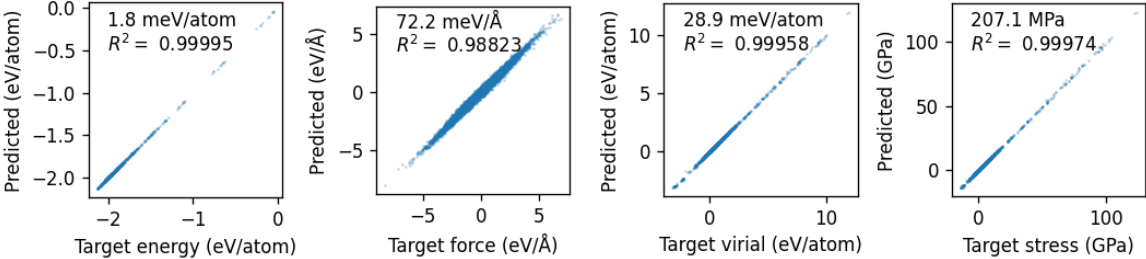


Figure S2: Parity plot for the HSE06 model. Structures for which the stress tensors have not been evaluated with DFT are not included in the virial and stress tensor parity plots.

## Comparison of phonon dispersion predicted from DFT and NEP

The 0 K harmonic phonon spectra for  $\text{BaZrS}_3$  in its three observed phases are displayed. The dashed black line corresponds to that generated with our NEP model, the solid blue is calculated using DFT-calculated forces. The largest discrepancies correspond to high-frequency modes strongly associated with the sulfur species.<sup>21</sup>

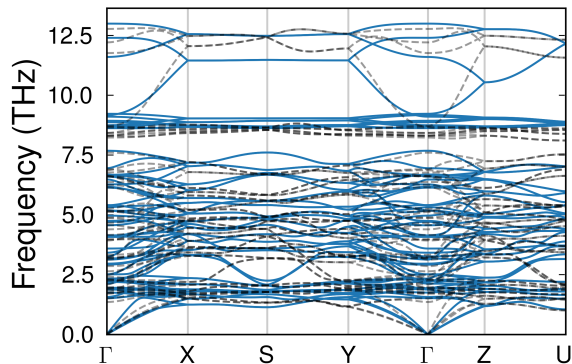


Figure S3: Pnma DFT (solid blue) vs NEP (dashed black) phonons

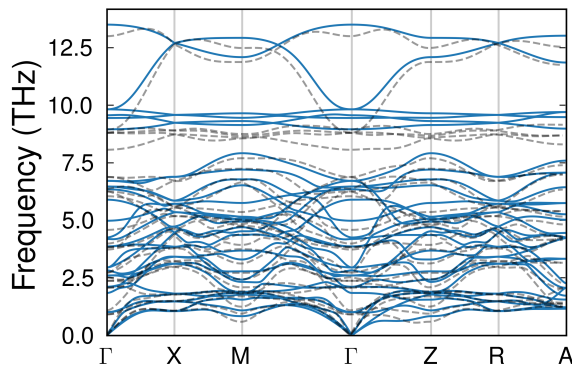


Figure S4: I4/mcm DFT (solid blue) vs NEP (dashed black) phonons

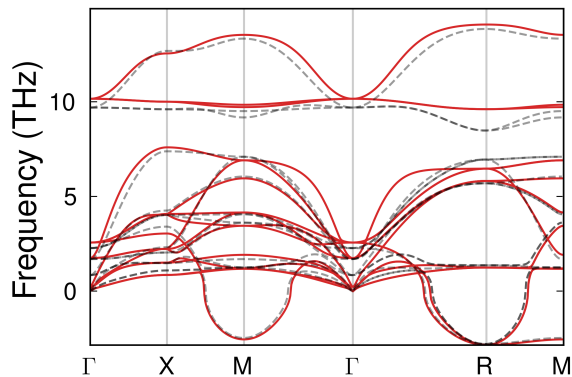


Figure S5: Pm $\bar{3}$ m DFT (solid red) vs NEP (dashed black) phonons

# Mode projections for Glazer tilt structures

In our comprehensive evaluation of all 15 Glazer-tilted structures we observe that  $I4/mcm$  and its subgroups ( $P4_2/nmc$ ,  $Cmcm$ ,  $C2/m$ ,  $C2/c$ ,  $P\bar{1}$ ) have similar energies according to DFT calculations and the NEP model. Our workflow for constructing these structures was to constrain the spacegroup symmetry using the ASE<sup>5</sup> FIXSYMMETRY function. Subgroup structures which are unstable at 0 K relax to their supergroup phase with a small (but non-zero) phonon mode amplitude. The corresponding distortion lies within the tolerance factor of the symmetry-constrained relaxation ( $10^{-5}$  Å). This small difference in structure results in energies that are similar but not exactly the same. For example, the  $Cmcm$   $a^0b^+c^-$  structure relaxes to an  $I4/mcm$   $a^0b^0c^-$  equivalent structure with a small mode projection value for the  $b^+$  tilt. This results in a small energy difference (0.2 meV) between the two phases.

Similar observations can be made for the  $P2_1/m$  and  $Pnma$  phases, and the  $Immm$  and  $P4/mbm$  phases.

Space group	$M_x$	$M_y$	$M_z$	$R_x$	$R_y$	$R_z$
$Pm\bar{3}m$ (221)	0.000000	0.000000	-0.000000	-0.000000	0.000000	0.000000
$I4/mcm$ (140)	0.000000	0.000000	0.000000	0.000000	0.000000	0.575006
$P4/mbm$ (127)	0.000000	0.000000	0.548092	0.000000	0.000000	0.000000
$Imma$ (74)	0.000000	0.000000	0.000000	0.000000	0.373962	0.373962
$C2/m$ (12)	0.000000	0.000000	0.000000	0.000000	0.000030	0.575030
$Cmcm$ (63)	0.000000	0.000002	0.000000	0.000000	0.000000	0.575030
$I4/mmm$ (139)	0.000000	0.328544	0.328544	0.000000	0.000000	0.000000
$R\bar{3}c$ (167)	0.000000	0.000000	0.000000	0.292519	0.292519	0.292519
$C2/c$ (15)	0.000000	0.000000	0.000000	0.575000	0.000016	0.000016
$P\bar{1}$ (2)	0.000000	0.000000	0.000000	0.574996	0.000037	0.000017
$I4/mmm$ (139)	0.000000	0.328544	0.328544	0.000000	0.000000	0.000000
$Pnma$ (62)	0.401595	0.000000	0.000000	0.000000	0.321830	0.321830
$P2_1/m$ (11)	0.401610	0.000000	0.000000	0.000000	0.321820	0.321830
$P4_2/nmc$ (137)	0.000001	0.000001	0.000000	0.000000	0.000000	0.575031
$Im\bar{3}$ (204)	0.251797	0.251797	0.251797	0.000000	0.000000	0.000000
$Immm$ (71)	0.548063	0.000001	0.000003	0.000000	0.000000	0.000000

Table S1: Mode projection on DFT relaxed geometries

Space group	$M_x$	$M_y$	$M_z$	$R_x$	$R_y$	$R_z$
$Pm\bar{3}m$ (221)	0.000000	0.000000	0.000000	0.000000	0.000000	0.000000
$I4/mcm$ (140)	0.000000	0.000000	0.000000	0.000000	0.000000	0.579234
$P4/mbm$ (127)	0.000000	0.000000	0.542603	0.000000	0.000000	0.000000
$Imma$ (74)	0.000000	0.000000	0.000000	0.000000	0.369080	0.369080
$C2/m$ (12)	0.000000	0.000000	0.000000	0.000000	-0.000028	0.579234
$Cmcm$ (63)	0.000000	0.000000	0.000000	0.000000	0.000000	0.579234
$I4/mmm$ (139)	0.000000	0.329391	0.329391	0.000000	0.000000	0.000000
$R\bar{3}c$ (167)	0.000000	0.000000	0.000000	0.286208	0.286208	0.286208
$C2/c$ (15)	0.000000	0.000000	0.000000	0.579234	0.000025	0.000025
$P\bar{1}$ (2)	0.000000	0.000000	0.000000	0.579233	0.000045	0.000011
$I4/mmm$ (139)	0.000000	0.329391	0.329391	0.000000	0.000000	0.000000
$Pnma$ (62)	0.400823	0.000000	0.000000	0.000000	0.326056	0.326056
$P2_1/m$ (11)	0.400821	0.000000	0.000000	0.000000	0.326061	0.326054
$P4_2/nmc$ (137)	0.000000	0.000000	0.000000	0.000000	0.000000	0.579234
$Im\bar{3}$ (204)	0.251378	0.251378	0.251378	0.000000	0.000000	0.000000
$Immm$ (71)	0.542603	0.000000	0.000000	0.000000	0.000000	0.000000

Table S2: Mode projection on NEP relaxed geometries

## Recovery of the orthorhombic phase during cooling at $-1$ GPa

Our cooling simulations in the main text do not recover the orthorhombic Pnma phase formed at 0 K. This stems from the numerical limitations of our simulations; the short timescales considered make a first-order transition (with associated kinetic barrier) from the tetragonal phase implausible. Here, we plot the heating and cooling runs at 1 GPa, where the orthorhombic phase is recovered around 560 K. This variation in our results is due to the stochastic nature of molecular dynamics simulations.

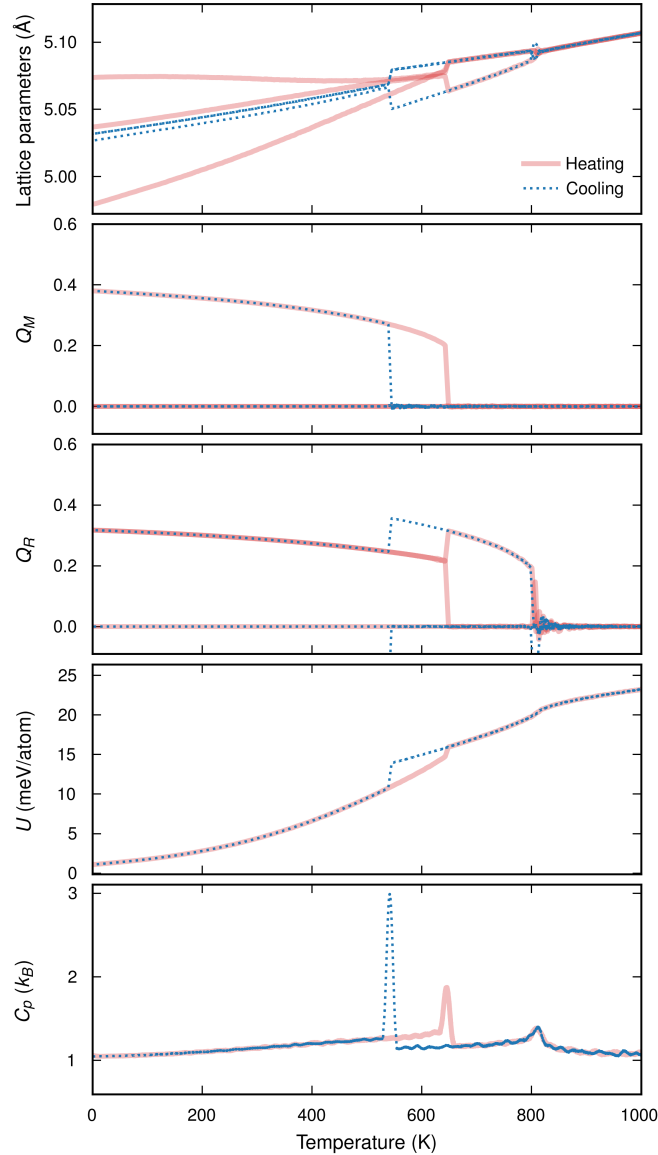


Figure S6: Heating and cooling runs at pressure  $-1$  GPa. The orthorhombic Pnma phase is recovered in the cooling run, unlike our simulations at 0 Pa (see the main text).

## Finite-temperature phonons from molecular dynamics

The DYNASOR package<sup>17</sup> is used to calculate the spectral energy density of the  $I4/mcm$  and  $Pm\bar{3}m$  phases at various temperatures.

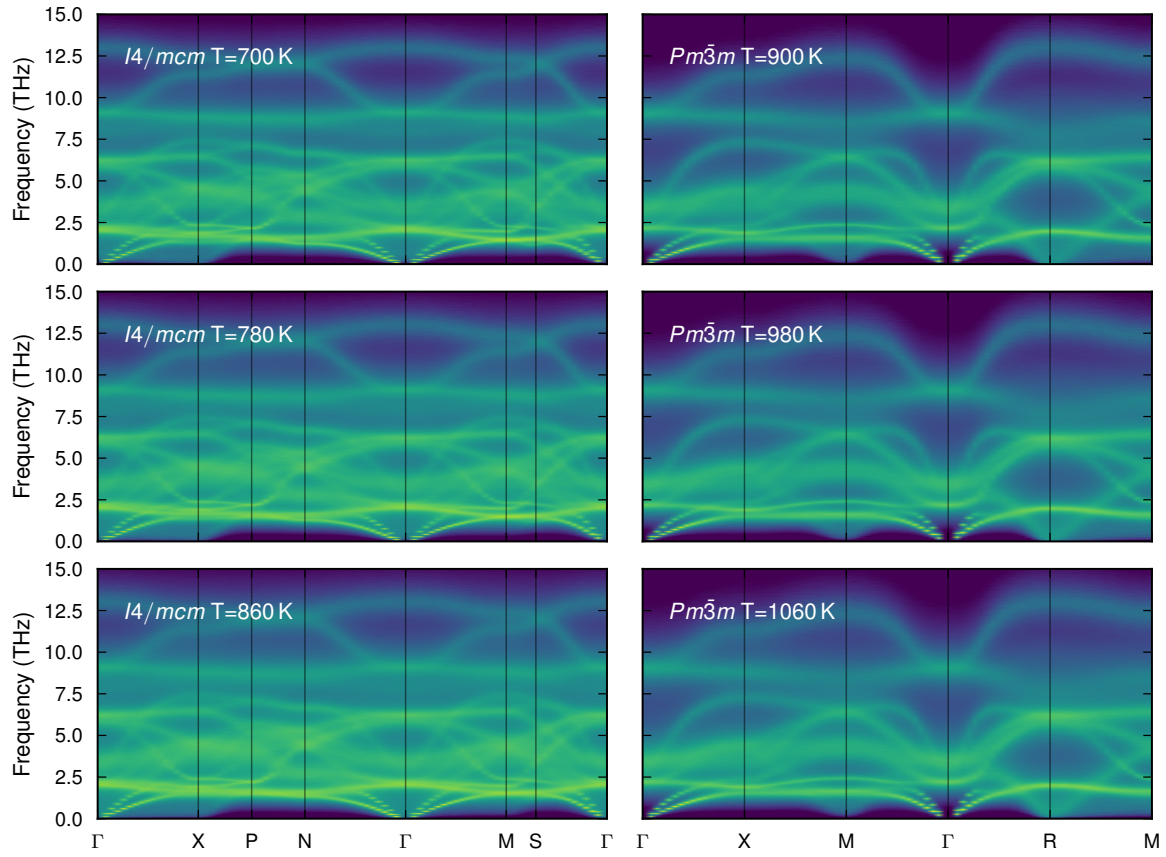


Figure S7: Spectral energy densities of the tetragonal  $I4/mcm$  and cubic  $Pm\bar{3}m$  phases of BaZrS<sub>3</sub>.

# Phase transition temperature using the harmonic approximation

Helmholtz free energies of the orthorhombic ( $Pnma$ ) and tetragonal ( $I4/mcm$ ) phases are evaluated within the harmonic approximation. The phase transition temperature with DFT-calculated phonon frequencies is 460 K, and with NEP-calculated frequencies it is 243 K. The phase transition temperature predicted with our fully anharmonic molecular dynamics model (see main text) is 610 K.

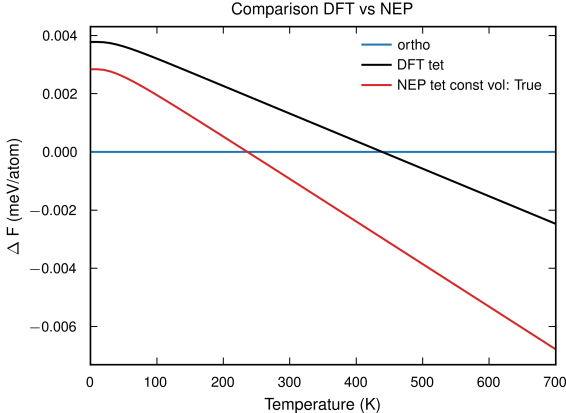


Figure S8: Helmholtz free energy difference between  $Pnma$  and  $I4/mcm$  phases ( $\Delta F$ ), calculated under the harmonic approximation.

## Perovskite bond compressibility

Perovskites with lower symmetry (more tilted) structures generally exhibit a series of octahedral tilt-driven phase transitions to higher symmetry (less tilted) structures with increasing temperature. The phase transition temperature  $T_c$  can increase or decrease with pressure,  $\frac{dT_c}{dP} > 0$  or  $\frac{dT_c}{dP} < 0$  respectively.<sup>22</sup> For BaZrS<sub>3</sub> we find  $\frac{dT_c}{dP} > 0$  (Fig 3 in the main text). This behaviour can be rationalised by considering the relative compressibility of the A-X and B-X bonds.<sup>22,23</sup> If the B-X bonds forming the octahedra are relatively rigid then pressure must induce tilting to accommodate the volume reduction, resulting in the compression of the A-X bonds and a reduction in symmetry. If the A-X bonds are relatively rigid then pressure must induce a reduction in the octahedral volume through compression of the B-X bond. The ratio of the B-X and A-X bond compressibilities ( $\frac{\beta_B}{\beta_A}$ ) can be used to indicate how the phase transition temperature will vary as a function of pressure:  $\frac{dT_c}{dP} > 0$  when  $\frac{\beta_B}{\beta_A} < 1$ , and  $\frac{dT_c}{dP} < 0$  when  $\frac{\beta_B}{\beta_A} > 1$ . The parameter  $M_i = \beta_i^{-1}$  is given by:

$$M_i = \frac{R_i N_i}{B} \exp\left(\frac{R_i - R_0}{B}\right) \quad (\text{S5})$$

where  $N_i$  is the coordination number,  $R_i$  average bond distance (to X-atoms),  $B$  is a constant with value 0.37, and  $R_0$  is the bond-valence parameter.<sup>24</sup> For BaZrS<sub>3</sub> we obtain  $\frac{\beta_B}{\beta_A} = \frac{M_A}{M_B} \approx 0.45$ . This indicates that  $\frac{dT_c}{dP} > 0$ , in agreement with our predicted phase diagram.

# Harmonic Raman spectra

The following harmonic Raman spectra analysis was performed using the phonopy-spectroscopy code.<sup>25</sup> Peak positions were evaluated assuming harmonic vibrational behaviour and using the PBEsol functional. Dielectric tensors were evaluated using the PBE functional. A light basis set with a minimum density of 5 k-grids per  $\text{\AA}^{-3}$  was used throughout. A Lorentzian of width  $0.05\text{cm}^{-1}$  is used to broaden the peaks.

BaZrS<sub>3</sub> in the the *Pnma* phase has 60 optic phonon modes, of which 24 are Raman active:  $\Gamma = 7A_g \oplus 5B_{1g} \oplus 7B_{2g} \oplus 5B_{3g}$ .

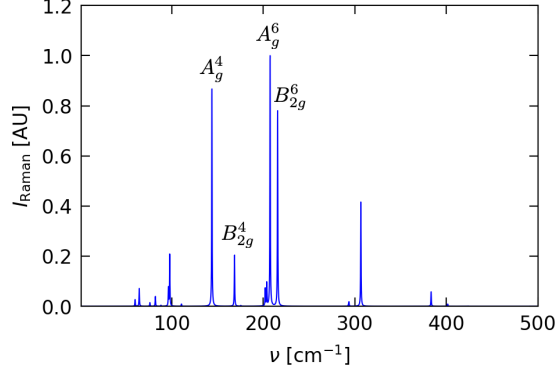


Figure S9: Harmonic first-order Raman spectra of the *Pnma* phase

Frequency [ $\text{cm}^{-1}$ ]	Intensity [ $\text{\AA}^4 \text{amu}^{-1}$ ]	Mode Symmetry
57.38246	31.294167	$A_g$
62.740697	74.397711	$B_{2g}$
72.865691	20.712113	$A_g$
74.878717	0.428877	$B_{3g}$
79.451252	35.213175	$B_{2g}$
82.730798	4.047662	$B_{1g}$
89.396457	81.906317	$B_{2g}$
94.004782	202.648574	$A_g$
105.117071	8.151943	$B_{1g}$
139.776095	927.058612	$A_g$
157.205497	0.129784	$B_{3g}$
162.91409	192.607928	$B_{2g}$
166.327512	3.336429	$A_g$
171.34857	2.338391	$B_{1g}$
198.430549	98.18659	$B_{2g}$
200.803735	93.792521	$B_{3g}$
204.900935	1063.364972	$A_g$
213.109461	766.788035	$B_{2g}$
289.681849	19.314493	$B_{1g}$
289.943548	8.201392	$B_{3g}$
304.087743	361.586611	$A_g$
389.08038	48.066782	$B_{1g}$
400.954212	7.889141	$B_{2g}$
419.617256	0.634279	$B_{3g}$

Table S3: Raman frequencies and mode symmetries for the *Pnma* phase

BaZrS<sub>3</sub> in the  $I4/mcm$  phase has 30 optic phonon modes, of which 7 are Raman active:  $\Gamma = 3E_g \oplus A_{1g} \oplus 2A_{2g} \oplus B_{1g} \oplus B_{2g}$ .

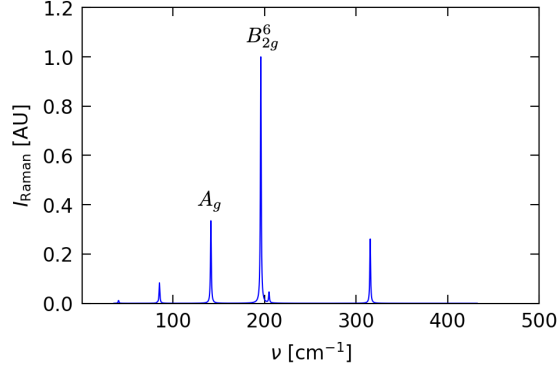


Figure S10: Harmonic first-order Raman spectra of the  $I4/mcm$  phase

Frequency [cm <sup>-1</sup> ]	Intensity [ $\text{\AA}^4 \text{amu}^{-1}$ ]	Mode Symmetry
40.762563	3.683262	E <sub>g</sub>
40.762563	3.687507	E <sub>g</sub>
42.565308	0.000000	A <sub>2u</sub>
69.245268	0.000000	E <sub>u</sub>
69.245268	0.000000	E <sub>u</sub>
83.275265	0.896384	E <sub>g</sub>
83.275265	0.894630	E <sub>g</sub>
85.401421	53.217047	B <sub>2g</sub>
100.908270	0.000000	E <sub>u</sub>
100.908270	0.000000	E <sub>u</sub>
126.898251	0.000000	E <sub>u</sub>
126.898251	0.000000	E <sub>u</sub>
137.013961	0.000000	A <sub>2u</sub>
141.559757	216.862006	A <sub>1g</sub>
155.032805	0.000000	B <sub>1u</sub>
196.069483	645.987936	B <sub>2g</sub>
205.046737	13.904421	E <sub>g</sub>
205.046737	13.919185	E <sub>g</sub>
207.325511	0.000000	A <sub>1u</sub>
230.492719	0.000000	E <sub>u</sub>
230.492719	0.000000	E <sub>u</sub>
281.507146	0.000044	A <sub>2g</sub>
302.441159	0.000000	A <sub>2u</sub>
303.618329	0.000000	E <sub>u</sub>
303.618329	0.000000	E <sub>u</sub>
315.495626	167.934156	B <sub>1g</sub>
427.229088	0.000392	A <sub>2g</sub>

Table S4: Raman frequencies and mode symmetries for the  $I4/mcm$  phase

BaZrS<sub>3</sub> in the  $Pm\bar{3}m$  phase has 15 optic phonon modes however, due to Raman selection rules, none of the modes are first-order Raman active. Any Raman signal observed from this phase derive from second-order Raman effects.

## Static structure factor

X-ray scattering intensities are equivalent to static structure factors weighted with species- and source-dependent form factors. We demonstrate the effect of including the form factors through direct comparison in Fig. S11. A number of peaks are not present in the scattering intensity, most noticeably at a scattering angle of  $17.5^\circ$ .

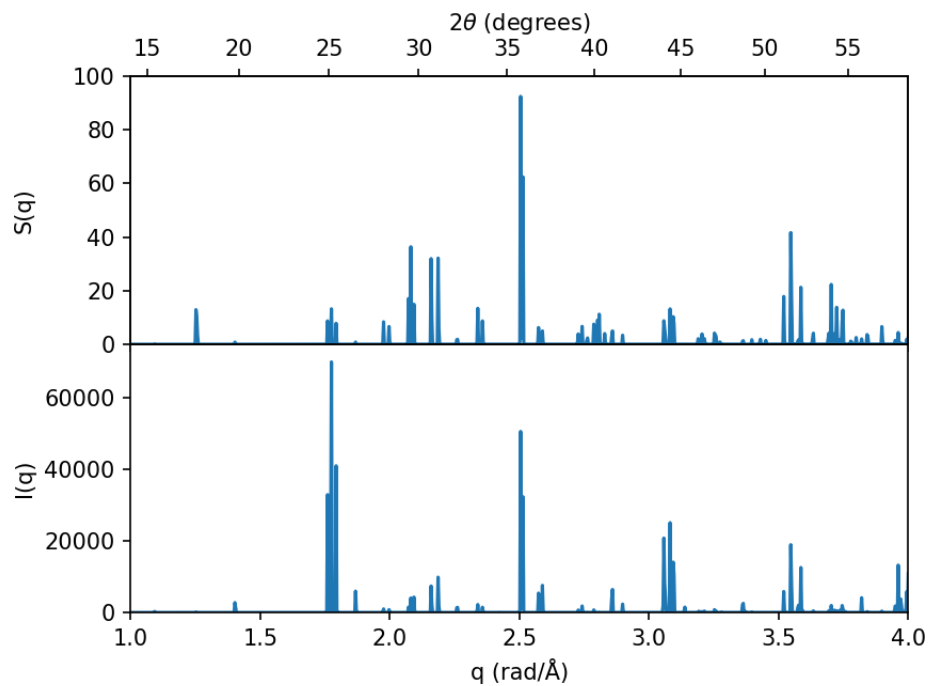


Figure S11: Comparison of the static structure factor pattern ( $S(q)$ ) to the x-ray diffraction pattern ( $I(q)$ ).

The temperature-dependent static structure factors are displayed in Fig. S12. In contrast to the main text, superlattice peaks up to the fifth Brillouin Zone are displayed.

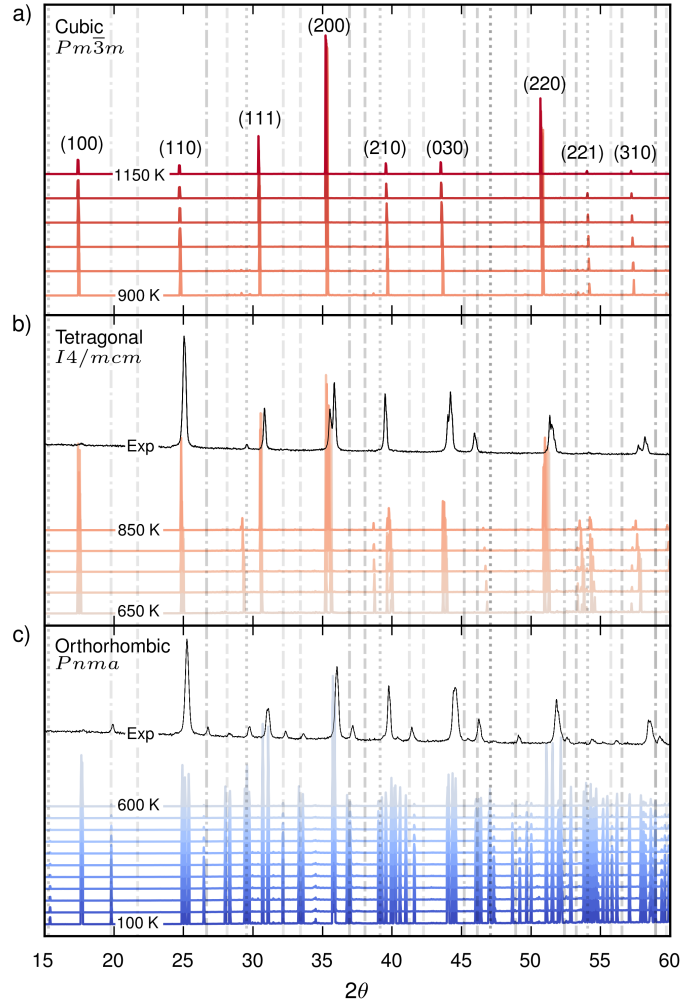


Figure S12: Static structure factor,  $S(q)$ , evaluated for three  $\text{BaZrS}_3$  polymorphs from 100 K to 1150 K in intervals of 50 K. A  $\text{Cu K}\alpha$  value of  $1.5406 \text{ \AA}$  was used for the  $q$  to  $\theta$  conversion. Cubic  $Pm\bar{3}m$  peaks are indexed. Superlattice peaks (up to the fifth Brillouin Zone) associated with R-, M- and X-point distortions are indexed and marked with dotted, dashed, and dash-dotted lines, respectively. Experimental XRD data of the orthorhombic (303 K) and tetragonal (923 K) phases from Ref. 26 are plotted in black.

# Partial static structure factors and X-ray diffraction scattering intensities

We can decompose the static structure factors for the various atom types in the system to compute partial static structure factors. In Fig. S13 we plot the partial structure factor of the  $Pnma$  phase at 300K and 0Pa. Similarly, we can decompose the X-ray diffraction scattering intensity  $I(q)$ . This is displayed in Fig. S14.

In Fig. S13 and Fig. S14 there is a peak at  $q = 1.4$  for the Ba-Ba partials. This corresponds to a distortion at the X-point which involves atomic displacement of the Ba species only.

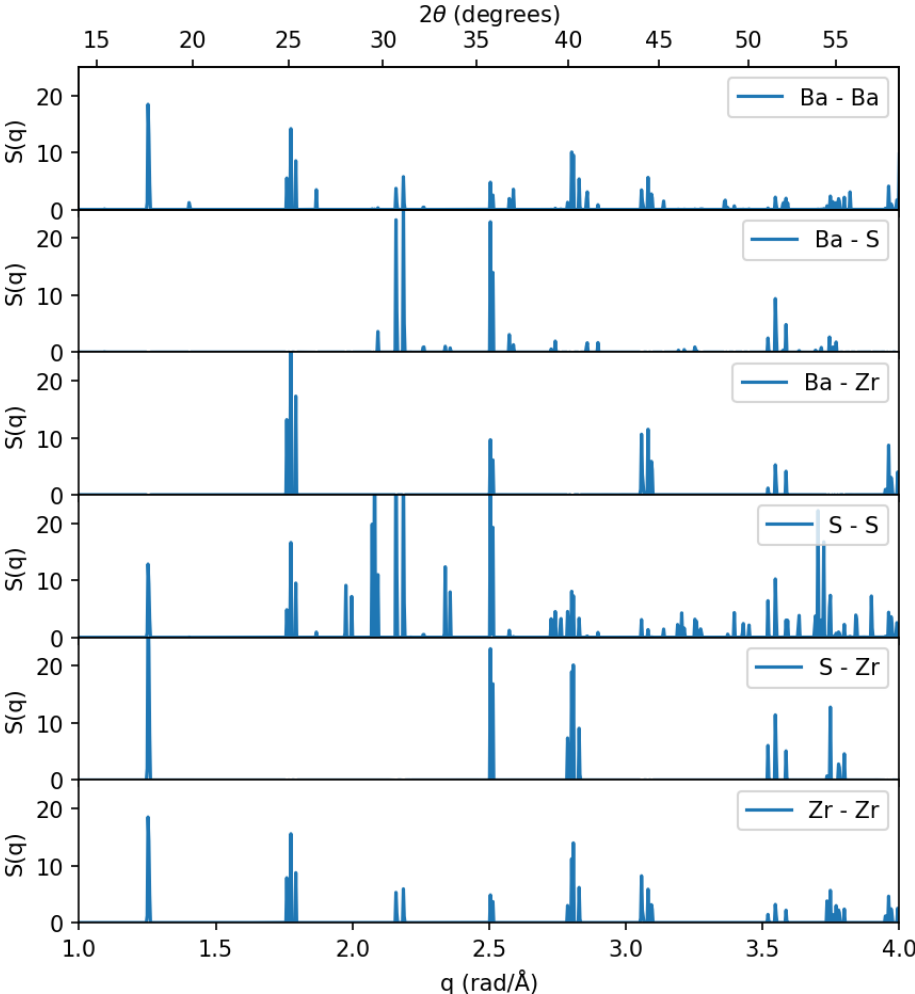


Figure S13: Partial static structure factors,  $S(q)$ , for  $BaZrS_3$  in the  $Pnma$  phase at 300 K and 0 Pa.

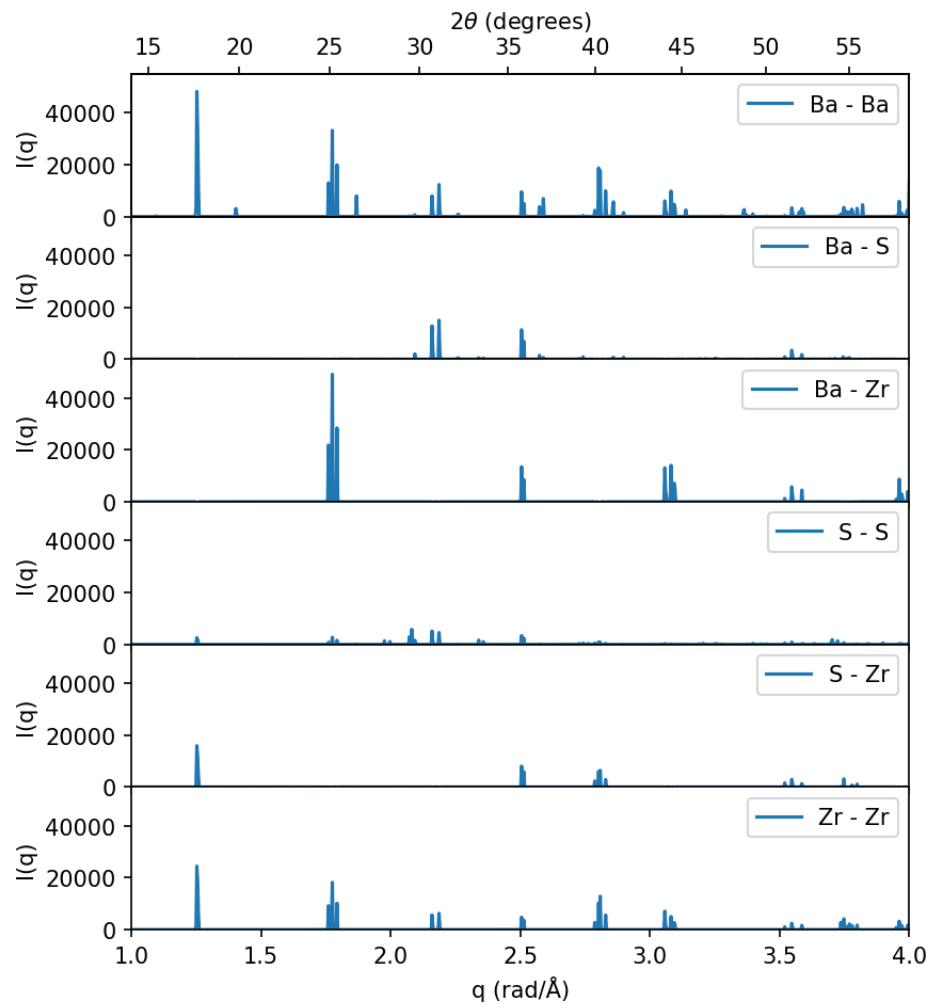


Figure S14: Partial scattering intensities,  $I(q)$ , for  $\text{BaZrS}_3$  in the  $Pnma$  phase at 300 K and 0 Pa.

## Supplemental References

- [1] E. Fransson, J. Wiktor, and P. Erhart, Phase transitions in inorganic halide perovskites from machine learning potentials (2023), arXiv.2301.03497.
- [2] Z. Fan, Z. Zeng, C. Zhang, Y. Wang, K. Song, H. Dong, Y. Chen, and T. Ala-Nissila, *Physical Review B* **104**, 104309 (2021).
- [3] Z. Fan, *Journal of Physics: Condensed Matter* **34**, 125902 (2022).
- [4] Z. Fan, Y. Wang, P. Ying, K. Song, J. Wang, Y. Wang, Z. Zeng, K. Xu, E. Lindgren, J. M. Rahm, A. J. Gabourie, J. Liu, H. Dong, J. Wu, Y. Chen, Z. Zhong, J. Sun, P. Erhart, Y. Su, and T. Ala-Nissila, *The Journal of Chemical Physics* **157**, 114801 (2022).
- [5] A. H. Larsen, J. J. Mortensen, J. Blomqvist, I. E. Castelli, R. Christensen, M. Dułak, J. Friis, M. N. Groves, B. Hammer, C. Hargus, E. D. Hermes, P. C. Jennings, P. B. Jensen, J. Kermode, J. R. Kitchin, E. L. Kolsbjerg, J. Kubal, K. Kaasbjerg, S. Lysgaard, J. B. Maronsson, T. Maxson, T. Olsen, L. Pastewka, A. Peterson, C. Rostgaard, J. Schiøtz, O. Schütt, M. Strange, K. S. Thygesen, T. Vegge, L. Vilhelmsen, M. Walter, Z. Zeng, and K. W. Jacobsen, *Journal of Physics: Condensed Matter* **29**, 273002 (2017).
- [6] E. Lindgren, M. Rahm, E. Fransson, F. Eriksson, N. Österbacka, Z. Fan, and P. Erhart, *Journal of Open Source Software* **9**, 6264 (2024).
- [7] F. Eriksson, E. Fransson, and P. Erhart, *Advanced Theory and Simulations* **2**, 1800184 (2019).
- [8] J. P. Perdew, A. Ruzsinszky, G. I. Csonka, O. A. Vydrov, G. E. Scuseria, L. A. Constantin, X. Zhou, and K. Burke, *Physical review letters* **100**, 136406 (2008).
- [9] A. V. Krukau, O. A. Vydrov, A. F. Izmaylov, and G. E. Scuseria, *J. Chem. Phys.* **125**, 224106 (2006).
- [10] V. Blum, R. Gehrke, F. Hanke, P. Havu, V. Havu, X. Ren, K. Reuter, and M. Scheffler, *Computer Physics Communications* **180**, 2175 (2009).
- [11] F. Knoop, T. Purcell, M. Scheffler, and C. Carbogno, *The Journal of Open Source Software* **5** (2020).
- [12] A. Togo, *Journal of the Physical Society of Japan* **92**, 012001 (2023).
- [13] Z. Fan, W. Chen, V. Vierimaa, and A. Harju, *Computer Physics Communications* **218**, 10 (2017).
- [14] D. Frenkel and A. J. C. Ladd, *The Journal of Chemical Physics* **81**, 3188 (1984).
- [15] R. Freitas, M. Asta, and M. de Koning, *Computational Materials Science* **112**, 333 (2016).
- [16] J. G. Kirkwood, *The Journal of Chemical Physics* **3**, 300 (1935).
- [17] E. Fransson, M. Slabanja, P. Erhart, and G. Wahnström, *Advanced Theory and Simulations* **4**, 2000240 (2021).
- [18] D. Waasmaier and A. Kirfel, *Acta Crystallographica Section A Foundations of Crystallography* **51**, 416–431 (1995).
- [19] E. Fransson, P. Rosander, F. Eriksson, J. M. Rahm, T. Tadano, and P. Erhart, *Communications Physics* **6**, 173 (2023).
- [20] A. Togo and I. Tanaka, *Scripta Materialia* **108**, 1 (2015).
- [21] Y. Wu, Y. Chen, Z. Fang, Y. Ding, Q. Li, K. Xue, H. Shao, H. Zhang, and L. Zhou, *The Journal of Physical Chemistry Letters* **14**, 11465 (2023).
- [22] R. J. Angel, J. Zhao, and N. L. Ross, *Physical review letters* **95**, 025503 (2005).

- [23] J. Zhao, N. L. Ross, and R. J. Angel, *Journal of Physics: Condensed Matter* **16**, 8763 (2004).
- [24] I. D. Brown and D. Altermatt, *Acta Crystallographica Section B* **41**, 244 (1985).
- [25] J. M. Skelton, L. A. Burton, A. J. Jackson, F. Oba, S. C. Parker, and A. Walsh, *Physical Chemistry Chemical Physics* **19**, 12452 (2017).
- [26] R. Bystrický, S. K. Tiwari, P. Hutár, and M. Sýkora, *Inorganic Chemistry* **63**, 12826 (2024).